

The UTMOST pulsar timing programme II: Timing noise across the pulsar population

M. E. Lower,^{1,2*} M. Bailes,^{1,3} R. M. Shannon,^{1,3} S. Johnston,² C. Flynn,^{1,4} S. Osłowski,¹ V. Gupta,¹ W. Farah,¹ T. Bateman,⁵ A. J. Green,⁵ R. Hunstead,⁵ A. Jameson,^{1,4} F. Jankowski,⁶ A. Parthasarathy,^{1,2} D. C. Price,^{1,7} A. Sutherland,⁵ D. Temby,⁵ and V. Venkatraman Krishnan^{8,1,3}

¹Centre for Astrophysics and Supercomputing, Swinburne University of Technology, PO Box 218, Hawthorn, VIC 3122, Australia

²CSIRO Astronomy and Space Science, Australia Telescope National Facility, Epping, NSW 1710, Australia

³OzGrav: The ARC Centre of Excellence for Gravitational-wave Discovery, Hawthorn VIC 3122, Australia

⁴ARC Centre of Excellence for All-sky Astrophysics (CAASTRO)

⁵Sydney Institute for Astronomy (SIfA), School of Physics, The University of Sydney, NSW 2006, Australia

⁶Jodrell Bank Centre for Astrophysics, Department of Physics and Astronomy, The University of Manchester, Manchester M13 9PL, UK

⁷Department of Astronomy, University of California Berkeley, 501 Campbell Hall, Berkeley CA 94720

⁸Max-Planck-Institut für Radioastronomie, Auf dem Hügel 69, D-53121 Bonn, Germany

Accepted XXX. Received YYY; in original form ZZZ

ABSTRACT

While pulsars possess exceptional rotational stability, large scale timing studies have revealed at least two distinct types of irregularities in their rotation: red timing noise and glitches. Using modern Bayesian techniques, we investigated the timing noise properties of 300 bright southern-sky radio pulsars that have been observed over 1.0–4.8 years by the upgraded Molonglo Observatory Synthesis Telescope (MOST). We reanalysed the spin and spin-down changes associated with nine previously reported pulsar glitches, report the discovery of three new glitches and four unusual glitch-like events in the rotational evolution of PSR J1825–0935. We develop a refined Bayesian framework for determining how red noise strength scales with pulsar spin frequency (ν) and spin-down frequency ($\dot{\nu}$), which we apply to a sample of 280 non-recycled pulsars. With this new method and a simple power-law scaling relation, we show that red noise strength scales across the non-recycled pulsar population as $\nu^a |\dot{\nu}|^b$, where $a = -0.84^{+0.47}_{-0.49}$ and $b = 0.97^{+0.16}_{-0.19}$. This method can be easily adapted to utilise more complex, astrophysically motivated red noise models. Lastly, we highlight our timing of the double neutron star PSR J0737–3039, and the rediscovery of a bright radio pulsar originally found during the first Molonglo pulsar surveys with an incorrectly catalogued position.

Key words: methods: data analysis – ephemerides – astrometry – stars: neutron – pulsars: general.

1 INTRODUCTION

The pulsar timing programme of the UTMOST¹ project (Bailes et al. 2017) monitors more than 400 pulsars using the upgraded Molonglo Observatory Synthesis telescope. This programme runs in parallel with searches for undiscovered pulsars and single pulses from rotating radio transients (RRATs), and Fast Radio Bursts (FRBs). These searches have already led to the discovery of thirteen FRBs (Caleb et al. 2017; Farah et al. 2018, 2019; Gupta et al. 2019a,b,c,d) and the intermittent pulsar candidate PSR J1659–54 (Venkatraman Krishnan et al. 2020).

As part of the timing programme, updated rotational models for 205 pulsars were published in the first paper of this series (Jankowski et al. 2019) and 9 pulsar glitches have been reported so far (Jankowski et al. 2015a,b, 2016, 2017; Lower et al. 2018, 2019).

While pulsars are renowned for their capacity to be used as astrophysical clocks, many have been observed to exhibit an intrinsic ‘timing noise’ in the measured arrival times of their pulses. Timing noise – stochastic wandering in observed pulse arrival times – manifests as either a ‘white’ noise processes if the power is distributed normally across all fluctuation frequencies, or ‘red’ noise if the timing residuals are dominated by low-fluctuation frequency structures. White timing noise can arise from instrumental artefacts,

* E-mail: mlower@swin.edu.au

¹ Not an acronym.

unaccounted radio frequency interference (RFI) and pulse-to-pulse shape variations, often referred to as pulse jitter (Staelin & Reifeisen 1968; Jenet et al. 1998). While fluctuations in the density of the interstellar medium along the line of sight (Keith et al. 2013), and the passage of nanohertz frequency gravitational waves (Detweiler 1979; Hellings & Downs 1983) manifest themselves as red noise in pulsar timing residuals, the dominant source of intrinsic red noise over long timescales is believed to arise from irregularities in pulsar rotation. One of two primary sources of rotational irregularities are pulsar glitches, discrete spin-up events that often decay exponentially over the following months to years. Glitches are posited to originate from either the release of built up tension within the neutron star’s crust via starquakes (Ruderman 1969; Baym et al. 1969), or the unpinning of superfluid vortices from the crustal lattice (Anderson & Itoh 1975; Alpar et al. 1985; Melatos et al. 2008). The other main type of rotational irregularity is ‘spin noise’, long-term variations in pulsar spins characterized by a red power spectrum (hereafter referred to as red noise). While red noise is distinct from glitches, it may be possible that glitch recoveries and switching between emission/spin-down states contributes to the overall red noise seen in some pulsars. The nature of the relationship between glitches and red noise is also open for debate (Hobbs et al. 2010; Parthasarathy et al. 2019).

While the precise mechanism behind pulsar red noise is unknown, potential external causes include fluctuations in the spin-down torque (Cheng 1987a), free-precession (Stairs et al. 2000; Brook et al. 2014; Kerr et al. 2016), asteroid belts or debris disks interacting with the pulsar magnetic field (Cordes & Shannon 2008), undetected planetary companions (Kerr et al. 2015), changes in pulse shape (Brook et al. 2016) and discrete quasi-periodic magnetospheric state switching (Kramer et al. 2006a; Lyne et al. 2010). Internal mechanisms such as the outward exchange of angular momentum due to coupling between the outer crust and superfluid interior (Jones 1990), undetected micro-glitches (Cheng 1987b), vortex re-pinning during glitch recovery (Melatos et al. 2008) and superfluid turbulence (Greenstein 1970; Link 2012; Cordes & Shannon 2008) have also been proposed as mechanisms behind red noise. Long-term studies of large samples of pulsars by Hobbs et al. (2005) and Hobbs et al. (2010) found red noise is common across the pulsar population, and claimed pure random walks in pulsar phase, spin frequency or spin-down rate cannot accurately model the observed structures in the timing residuals (Cordes & Downs 1985). However, Shannon & Cordes (2010) showed that if the random walk step-sizes are drawn from a power-law function (rather than a Gaussian), then most red noise structures can be replicated.

In this paper we undertake a study of the rotational properties of 300 pulsars that have been observed over the past 1.0-4.8 years by UTMOST. This includes a full reanalysis of nine previously reported glitches (Jankowski et al. 2015a,b, 2016, 2017; Espinoza et al. 2011; Sarkissian et al. 2017; Palfreyman et al. 2018; Lower et al. 2018; Liu et al. 2019; Sarkissian et al. 2019; Kerr 2019), while accounting for the effects of timing noise and the discovery of two new glitches. To parameterize the effects of red noise on the timing residuals, and to avoid biasing our measurements of pulsar spin and spin-down, we employ the Bayesian pulsar timing software TEMPO_{NEST} (Lentati et al. 2014). We search for correlations between pulsar properties and red noise strength, in addition to how it scales as a function of spin and spin-down frequencies across the population.

In Section 2 we outline the observing and data processing strategies. In Section 3 we describe the phenomenology behind characterising pulsar timing noise and the statistical framework we use to parameterise red timing noise and perform simultaneous

measurements of pulsar spin properties. We report on our updated timing models and present the results of our red noise search and glitch analysis in Section 4. In Section 5 we examine potential links between red noise strength and pulsar properties, in addition to outlining and comparing a new, robust method for determining how timing noise scales across the population. Lastly, in Section 6 we draw our conclusions and comment on future applications of our Bayesian framework.

2 OBSERVATIONS

2.1 System overview

The UTMOST project began with the backend upgrade to the refurbished Molonglo Observatory Synthesis Telescope (Bailes et al. 2017). MOST is a Mills-Cross design aperture synthesis telescope situated approximately 35 km South-East of Canberra, Australia. It is comprised of two 778 m long East-West arms that can be slewed in the north-south direction, and a static North-South arm, that is being re-engineered as part of the UTMOST-2D project (Day et al. in prep.). The telescope operates at a central frequency of 835 MHz² covering a bandwidth of 31.25 MHz. The ring-shaped design of the antenna elements means the instrument is mainly sensitive to right-hand circularly polarized emission.

For the first two years of the timing programme we were capable of mechanically tracking sources in hour angle on the sky. However, maintenance issues and an associated degradation of performance ultimately led us to convert the telescope into a meridian transit instrument in June 2017. While we are no longer able to track sources mechanically, we are able to electronically track up to four pulsars simultaneously as they transit the telescope’s 4° × 2° primary beam. A typical timing observation lasts between 5-20 minutes depending on the brightness of the pulsar and whether it displays interesting behaviours (e.g. emission state-switching). Observations are usually performed autonomously via the scheduler developed for the UTMOST multi-epoch Survey of Magnetars, Intermittent pulsars, RRATs and FRBs (SMIRF: Venkatraman Krishnan et al. 2020), which has improved the efficiency of the timing programme since its June 2017 introduction. Manual observations of targets of interest, phase calibrators and long FRB transit searches are usually performed using the AUTOMATIC MODE scheduler detailed in Jankowski et al. (2019).

2.2 Radio frequency interference

Observations conducted by UTMOST are often contaminated by radio frequency interference (RFI) as its frequency band is shared by radio transmissions from two Australian mobile telecommunications providers. As the telescope is an array, voltage addition in phase only occurs for radio emitting sources that are more than a Fresnel scale away (~ 10000 km) from the telescope, while anything closer is attenuated. Although this does reduce the overall amount of observed RFI, it is still prevalent in a significant fraction of observations. Removal of RFI is performed by passing the data through an excision pipeline that involves spectral kurtosis prior to folding of the raw data with `DSPSR`³ (van Straten & Bailes 2011), followed by median filtering of the folded archives via the tools

² The sensitivity of the MOST peaks at ~ 843 MHz, as this is where the resonant cavities are tuned to.

³ [dspsr.sourceforge.net](https://github.com/dspsr/dspsr)

in PSRCHIVE⁴ (Hotan et al. 2004; van Straten et al. 2012). Manual RFI removal with PSRCHIVE’s interactive PAZI tool is undertaken when necessary. More recently, we have modified the RFI cleaning pipeline to use CLFD⁵ (Morello et al. 2018), which uses Tukey’s rule to find and zero-weight data corresponding to outliers in the standard deviation, peak-to-peak difference and second bin of the Fourier transform of each sub-integration and channel of a folded observation. This alone has improved the timing accuracy of many slow pulsars we observe by a factor of two. The amount of data lost to RFI excision is typically on the order of 5 percent, but can be as high as 10 to 15 percent during times of high road traffic (and hence an increased number of mobile handsets) near the telescope.

2.3 Pulsar-timing dataset

We began the pulsar-timing programme during October 2015 after phasing of the telescope became routine. Limited pulsar observations prior to this date were undertaken while the telescope was still undergoing upgrades and commissioning, but are largely of lower quality when compared to more recent data. A general overview of the UTMOST timing programme can be found in Jankowski et al. (2019), which includes the first scientific results of the timing programme: a study of pulsar proper motions, transverse velocities, pulse duty cycles and flux densities at 843 MHz, and updated rotational and astrometric parameters for 205 pulsars. Currently we perform regular radio monitoring and timing of 412 pulsars, each of which was selected from an initial list of every pulsar for which an observation had been attempted by UTMOST. This includes monitoring the pulsed radio emission of two radio loud magnetars, PSR J1622–4950 and XTE J1810–197. Each pulsar observation typically lasts between 5–20 minutes, depending on the source flux density and declination. After RFI excision, the observations are then summed in frequency and time to produce averaged pulse profiles. These are then cross-correlated with a standard profile, a template generated from a smoothed, high signal-to-noise profile obtained after many hours of integration, to measure the pulse time of arrival (ToA) at the telescope (Taylor 1992). This ‘topocentric’ ToA is then converted to the ToA at the Solar System Barycentre via the Jet Propulsion Laboratory’s DE430 planetary ephemeris (Folkner et al. 2014). Due to sensitivity limitations of the telescope, most of these pulsars are bright, isolated southern pulsars with relatively long rotation periods. Their basic observational parameters are drawn from the Australia Telescope National Facility (ATNF) pulsar catalogue (PSRCAT; Manchester et al. (2005)⁶ and Jankowski et al. (2019), where the spin period, position and DM determination epoch is MJD 57600. Fig. 1 shows the spin period/period-derivative ($P-\dot{P}$) diagram for the full set of pulsars regularly monitored by UTMOST.

The cadence with which we observe individual pulsars varies from days to months, depending on their physical properties, and whether they exhibit interesting behaviour such as nulling, glitches or mode-changing. Precise observation cadences and lengths are defined by a pulsar’s position in the sky, apparent brightness and the scientific benefit of performing observations with daily to monthly cadences. We provide this information to SMIRF, which autonomously schedules and performs the observations. Limiting

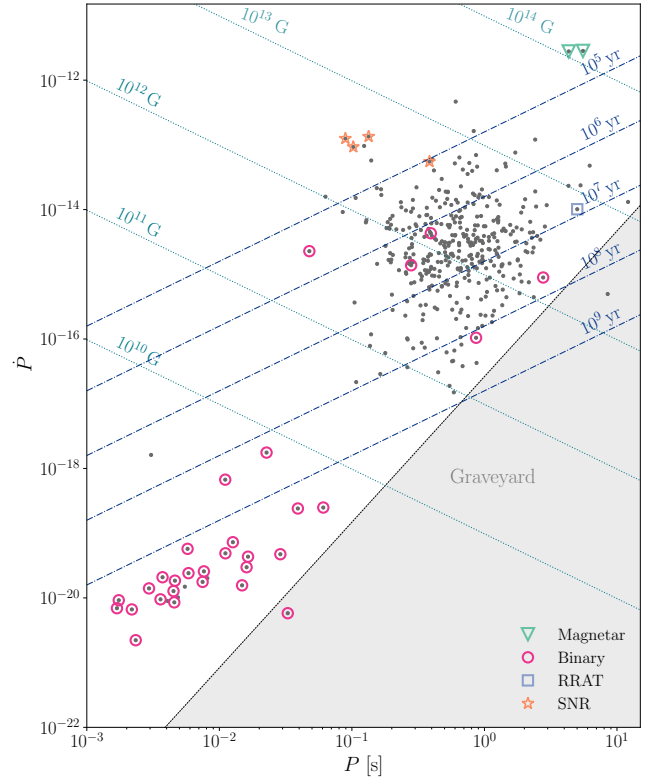


Figure 1. Period, period-derivative diagram for all pulsars regularly monitored by UTMOST. Pulsars residing in binary systems are highlighted by red circles. The RRAT PSR J2033+0042 is indicated by a blue square and the radio-loud magnetars PSR J1622–4950 and XTE J1810–197 by green triangles. Pulsars associated with supernova remnants are highlighted with stars. Lines of constant characteristic age are defined by the dash-dotted lines and constant surface magnetic field strength by dotted lines.

the amount of mechanical wear on the telescope due to slewing is also factored into how often particular pulsars are observed.

3 PULSAR-TIMING STRATEGY

To determine the timing properties of a pulsar, we must first establish a phase-connected timing solution. Pulsars that have undergone glitches or exhibit excess structures due to timing noise are difficult to solve coherently over long timing baselines, often requiring the addition of discrete phase jumps before updating the timing model. Once we have a phase coherent solution, we use TEMPO2 (Hobbs et al. 2006) to assign relative pulse numbers to each ToA, which we then track to avoid phase wraps when attempting to update the timing model. The effects of timing noise can be mitigated by including fits for higher order polynomials, corresponding to higher order spin-derivatives, into the timing model, or by subtracting a series of harmonically related sinusoids (e.g. FITWAVES in TEMPO2; Hobbs et al. (2006)). While these methods are useful for pre-whitening the timing residuals, they assume the measured pulsar properties and timing noise are uncorrelated. Attempts to avoid biases induced by correlations in the timing residuals include using a transform of the covariance matrix based on Cholesky decomposition to whiten the timing residuals (Coles et al. 2011), which enables the timing residual power spectrum to be fit by a steep red power-law. However, this method requires some *a priori* knowledge of the covariance matrix, and that the correlated timing noise process is stationary in the post-

⁴ psrchive.sourceforge.net

⁵ github.com/v-morello/clfd

⁶ www.atnf.csiro.au/research/pulsar/psrcat/

fit timing residuals. [van Haasteren & Levin \(2013\)](#) showed that the assumption of stationarity breaks down during the fitting process, leading to incorrect uncertainties on the spectrum estimates, and an incorrect covariance matrix for the pulsar timing model. They instead proposed the use of a Bayesian analysis, in which the stochastic timing noise and pulsar properties are modelled simultaneously, avoiding the possibility of biases in the final posterior distributions. This method, in particular the ability to perform model selection, was improved by [Lentati et al. \(2013\)](#) and [Lentati et al. \(2014\)](#), as the [van Haasteren & Levin \(2013\)](#) method is hampered by large matrix inversions and a growing parameter space as the timing model is linearized.

3.1 Phenomenological timing noise model

To model the effects of red timing noise, we utilized the phenomenology outlined in [Lentati et al. \(2014\)](#) and [Lentati et al. \(2016\)](#), where the power spectral density of the red noise process is described in the Fourier domain by a power law⁷ with amplitude A (in units of $\text{yr}^{3/2}$) and spectral index β

$$P_r(f) = \frac{A^2}{12\pi^2} \left(\frac{f}{f_{\text{yr}}}\right)^{-\beta}. \quad (1)$$

In addition to the standard power-law model, we also consider a variation of the spectral turnover model of [Coles et al. \(2011\)](#)

$$P_r(f) = \frac{A^2}{12\pi^2} \frac{(f_c/f_{\text{yr}})^{-\beta}}{[1 + (f/f_c)^{-\beta/2}]^2}, \quad (2)$$

where f_c is the frequency at which the spectrum turns over. While the models we test are phenomenological rather than drawn from physical theory, models of superfluid turbulence within neutron star interiors ([Melatos & Link 2014](#)), or the presence of circum-pulsar asteroid belts ([Cordes & Shannon 2008](#)) predict spectral flattening or turnovers in power spectra of pulsar timing residuals.

Excess white noise in the residuals due to pulse jitter or radio interference can be accounted for by modifying the uncertainties of individual ToAs as

$$\mu_i = \sigma_q^2 + F\sigma_i. \quad (3)$$

Here σ_i is the ToA uncertainty on the i -th observation derived from the cross-correlation procedure for generating ToAs, F is a fitting factor (commonly referred to as EFAC) that encodes the contribution of unaccounted instrumental effects and imperfect estimates of ToA uncertainties, while σ_q (error in quadrature: EQUAD) accounts for any additional sources of time-independent uncertainties (e.g pulse jitter).

3.2 Bayesian framework

To characterise timing noise and obtain accurate timing models, we used Bayesian parameter estimation to construct posterior probability distributions for the deterministic and stochastic pulsar properties θ from the timing residuals r . Prior to performing parameter estimation we first obtained an initial timing solution from previously computed models. In most cases, the initial timing solutions are re-fitted versions of those found in [Jankowski et al. \(2019\)](#) or `PSRCAT` ([Manchester et al. 2005](#)). We fit pulsar parameters that are poorly

constrained using a χ^2 minimisation scheme with `TEMPO2` ([Hobbs et al. 2006](#); [Edwards et al. 2006](#)), resulting in a phase-connected timing solution.

We conducted parameter estimation on these timing models using the `TEMPO_NEST`⁸ Bayesian pulsar timing software developed by [Lentati et al. \(2014\)](#). `TEMPO_NEST` utilizes the nested sampling algorithm `MULTI_NEST` ([Skilling 2004](#); [Feroz & Hobson 2008](#); [Feroz et al. 2009](#)) to sample the posterior distributions of the parameters θ , given timing residuals r and a timing model \mathcal{M} , while analytically marginalizing over nuisance parameters. The general form of the posterior probability distribution is given by Bayes' theorem as

$$p(\theta|r, \mathcal{M}) = \frac{\mathcal{L}(r|\theta, \mathcal{M})\pi(\theta, \mathcal{M})}{\mathcal{Z}(r|\mathcal{M})}, \quad (4)$$

where $\mathcal{L}(r|\theta, \mathcal{M})$ is the likelihood function for the residuals given a timing model and model parameters (equation 21 of [Lentati et al. \(2014\)](#)), $\pi(\theta, \mathcal{M})$ is our prior knowledge, the ranges of which are listed in Table 1 and $\mathcal{Z}(r|\mathcal{M})$ is the Bayesian evidence, which is a single number representing the completely marginalized likelihood defined by

$$\mathcal{Z}(r|\mathcal{M}) = \int d\theta \mathcal{L}(r|\theta, \mathcal{M})\pi(\theta, \mathcal{M}). \quad (5)$$

To account for potential covariances when fitting for the parameters of interest, we included the sky-position of the pulsar as free parameters. However, any improvements in the sky-position uncertainty over the values output by `TEMPO2` would be marginal at best, as all pulsars in our sample have been timed for more than 1 yr. Hence, we treat the sky-position as a set of nuisance parameters, $\theta_n = \{\alpha, \delta\}$, that are analytically marginalized over to obtain the marginalized posterior distribution for the parameters of interest (θ_i), defined by

$$p(\theta_i|r, \mathcal{M}) = \int \prod_{n \neq i} d\theta_n \pi(\theta_n, \mathcal{M}) \mathcal{L}(r|\theta_i, \theta_n, \mathcal{M}). \quad (6)$$

Any glitch parameters in the timing model are also marginalized over, unless we are explicitly attempting to measure them. Neglecting to do so biases the recovered spectral index toward larger values (a steeper red spectrum). For computing posterior distribution confidence intervals we use the maximum likelihood statistics from `CHAINCONSUMER`⁹ ([Hinton 2016](#)).

After conducting parameter estimation, we can use the resulting Bayesian evidences to compare two or more competing hypotheses ($\mathcal{M}_1, \mathcal{M}_2$) by calculating the odds ratio

$$\mathcal{O}_{12} = \frac{\mathcal{Z}(r|\mathcal{M}_1) \Pi_1}{\mathcal{Z}(r|\mathcal{M}_2) \Pi_2}, \quad (7)$$

where Π_1/Π_2 is the *a-priori* odds of the two hypotheses. In our case the prior odds are unity as we assume uninformative priors throughout our analysis. This leaves us with an alternative model comparison metric known as the Bayes factor, which can be calculated as

$$B_{12} = \frac{\mathcal{Z}(r|\mathcal{M}_1)}{\mathcal{Z}(r|\mathcal{M}_2)} = \frac{\int d\theta_1 \mathcal{L}(r|\theta_1, \mathcal{M}_1)\pi(\theta_1, \mathcal{M}_1)}{\int d\theta_2 \mathcal{L}(r|\theta_2, \mathcal{M}_2)\pi(\theta_2, \mathcal{M}_2)}, \quad (8)$$

where θ_1, θ_2 are the parameters associated with models \mathcal{M}_1 and \mathcal{M}_2 respectively. In our analysis, the specific models we compared include:

⁷ The division by $12\pi^2$ comes from this power-law originally being derived from the one-sided power spectrum a stochastic gravitational-wave background would induce in pulsar timing residuals (e.g [Jenet et al. 2006](#))

⁸ github.com/LindleyLentati/TempoNest

⁹ github.com/samreay/ChainConsumer/

Table 1. Prior ranges on pulsar and timing noise parameters. Δ_{param} is the uncertainty returned by TEMPO2, T is length of each pulsar’s data set.

Parameter	Symbol [units]	Prior range	Prior type
Spin-frequency and derivatives	$\nu, \dot{\nu}, \ddot{\nu}$ [Hz, s ⁻² , s ⁻³]	$\pm x^* \times \Delta_{\text{param}}$	Uniform
White noise fitting factor	EFAC	(-1, 2)	Uniform
White noise error in quadrature	EQUAD [s]	(-10, 1)	log-Uniform
Red noise amplitude	A [yr ^{3/2}]	(-20, -3)	log-Uniform
Red noise spectral index	β	(0, 20)	Uniform
Red noise turn-over frequency	f_c [yr ⁻¹]	(0.01/ T , 10/ T)	log-Uniform
Glitch phase jump	$\Delta\phi$ [rotations]	(-10, 10)	Uniform
Permanent change in spin-frequency	$\Delta\nu_p$ [Hz]	(-12, -5)	log-Uniform
Change in spin-down	$\Delta\dot{\nu}_p$ [Hz ⁻²]	(-10 ⁻²⁰ , -10 ⁻⁹)	Uniform
Decaying change in spin-frequency	$\Delta\nu_d$ [Hz]	(-12, -5)	log-Uniform
Glitch recovery timescale	τ_d [days]	(0, 3000)	Uniform

* x lies between 100 – 100000 depending on the pulsar.

- White timing noise (WTN): fitting for deterministic pulsar parameters, EFAC and EQUAD only.
- Power-law red noise (PLRN): fitting for a power-law red noise model (equation 1) in addition to the WTN parameters.
- Power-law red noise with frequency turnover (PL+FC): includes a turnover in the red power spectrum (equation 2) plus WTN parameters.
- Second spin-frequency derivative (PLRN+F2): same as PLRN, but also fitting a cubic term to measure $\ddot{\nu}$.

The specific choice of a Bayes factor threshold when performing model selection is largely dependent on what one considers to be an acceptable false positive rate. For instance, a conservative Bayes factor threshold of $|\ln(\mathcal{B}_{12})| > 8$ (corresponding to a false positive rate of $\sim 1/3000$) is generally used in gravitational-wave astronomy (Thrane & Talbot 2019). A more common interpretation is outlined in Kass & Raftery (1995), where a Bayes factor of $\ln(\mathcal{B}_{12}) > 5$ (false positive rate $\sim 1/150$) is considered to be ‘very strong’ evidence for one hypothesis over the other. In this work we use the latter interpretation, as it has previously been used in pulsar model selection studies (e.g., Lentati & Shannon 2015; Reardon et al. 2019; Parthasarathy et al. 2019). In cases where neither model is significantly preferred over the other, i.e. for $|\ln(\mathcal{B}_{12})| < 1$, Occam’s razor tells us the least complicated model is preferred.

3.3 Braking indices

Over long timescales, the spin-down of a pulsar is often approximated by a power law of the form

$$\dot{\nu} = -K\nu^n, \quad (9)$$

where K is a scaling constant related to the pulsar moment of inertia and magnetic field structure (Gunn & Ostriker 1969) and n is the ‘braking index’. The value of the braking index is potentially an indicator of the physical process that dominates the torque acting to slow the rotation of the neutron star. For instance, a braking index of $n = 1$ arises if the spin-down is dominated by an out-flowing particle wind from the pulsar surface (Harding et al. 1999), $n = 3$ corresponds to magnetic-dipole radiation (e.g. Shapiro & Teukolsky 1983), and $n = 5$ would indicate the pulsar is spinning down due to some form of quadrupole radiation, such as gravitational waves (Bonazzola & Gourgoulhon 1996; Yue et al. 2007). Magnetic field evolution or a varying misalignment between the spin and magnetic axes are also predicted to result in $n < 3$ (Blandford & Romani 1988; Lyne et al. 2013). By taking the derivative of equation 9 and solving for n , we can infer the braking index of a pulsar by measuring its *second* spin-frequency derivative ($\ddot{\nu}$), giving

$$n = \frac{\nu\ddot{\nu}}{\dot{\nu}^2}. \quad (10)$$

Obtaining accurate measurements of $\ddot{\nu}$ is difficult, as measured values of $\ddot{\nu}$ in ‘old’ pulsars are not significantly different from zero. As with measuring ν and $\dot{\nu}$, not accounting for timing noise in the pulsar residuals when attempting to measure $\ddot{\nu}$ will lead to biased measurements, as $\ddot{\nu}$ is often highly correlated with timing noise.

3.4 Glitch parameter estimation

While the low frequency structures resulting from red noise affect the long term timing precision of pulsars, pulsar glitches result in neutron stars spinning-up on timescales of seconds (Ashton et al. 2019a). This causes a near-instantaneous difference between the observed ToAs and what is expected from the timing model. Some pulsars take days to months to recover toward their original pre-glitch spin frequency (and sometimes do not fully recover or over-recover). In general the change in rotational phase from a glitch can be expressed in terms of instantaneous, permanent changes in the pulsar spin (ν_p) and spin-down ($\dot{\nu}_p$), as well as the exponential spin recovery (ν_d) over time (τ_d)

$$\phi_g(t) = \Delta\phi + \Delta\nu_p(t - t_g) + \frac{1}{2}\Delta\dot{\nu}_p(t - t_g)^2 - \Delta\nu_d\tau_d e^{-(t-t_g)/\tau_d}. \quad (11)$$

If the precise epoch at which a glitch occurred (t_g) is poorly constrained then there can be some uncertainty in the precise number of pulsar rotations between the last pre-glitch and first post-glitch observations. Hence an unphysical phase jump ($\Delta\phi$) is frequently implemented to maintain a phase-connected timing solution. If the glitch epoch were known precisely, a phase jump would not be required. Glitch recovery is often associated with the re-pinning of superfluid vortices (Melatos et al. 2008). The degree to which a glitch recovers can be quantified by the recovery parameter $Q = \Delta\nu_d/\Delta\nu_g$, where $\Delta\nu_g = \Delta\nu_p + \Delta\nu_d$.

When fitting for pulsar glitches we include five parameters drawn from equation 11 that describe the change in pulsar spin and post-glitch recovery, $\{\Delta\phi, \Delta\nu_p, \Delta\dot{\nu}_p, \Delta\nu_d, \tau_d\}$, in addition to the red noise and spin parameters. For pulsars found to have undergone multiple glitches within our timing data, we fitted all of the relevant glitch parameters simultaneously in order to avoid introducing biases from incomplete glitch models when attempting to model them individually. We then marginalize over the instantaneous phase jump to account for uncertainties on the glitch epoch. We employed Bayesian model selection in cases where it is difficult

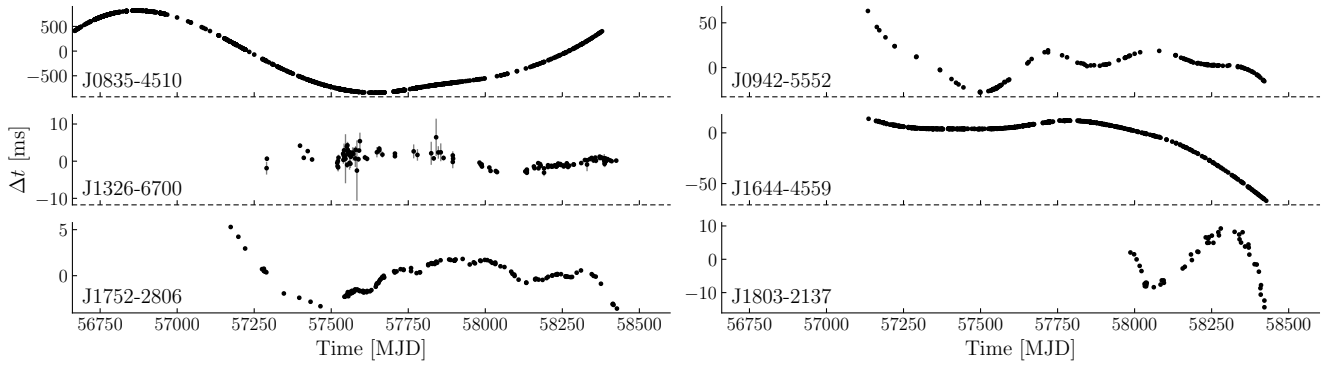


Figure 2. Phase connected timing residuals for 6 pulsars which exhibit various levels of red noise after fitting for ν and $\dot{\nu}$. Plots showing the timing residuals for all 300 pulsars can be found in the supplementary material.

to tell by eye whether a small glitch or glitch-like event is real, or is the result of a cusp in the residuals due to timing noise.

4 RESULTS

4.1 Updated timing models

Many pulsars in our sample have improved timing measurements over those from version 1.54 of the ATNF pulsar catalogue¹⁰, including a number that are not present in Jankowski et al. (2019). The updated astrometric and spin parameters are presented in Table A1. The resulting timing residuals for all pulsars analysed in this work are presented in Fig. 2. Ephemeris files in TEMPO2 format, ToAs, plots showing the one- and two-dimensional posterior distributions and a clock correction file are available to download from our online repository¹¹.

4.2 Spin frequency second derivatives and braking indices

By simultaneously modelling timing noise as a power-law process, we are able to search for unbiased values of $\ddot{\nu}$ by comparing Bayesian evidences for the power-law red noise (PLRN) and red noise with $\dot{\nu}$ (PLRN+F2) models. There are 8 pulsars in our sample that marginally prefer the PLRN+F2 model ($1 < \ln(\mathcal{B}) < 5$) for which we recover well constrained $\dot{\nu}$ posteriors that are inconsistent with zero. We find only one pulsar, PSR J0738–4042, significantly favours the PLRN+F2 model with a log Bayes factor > 5 , while PSR J1001–5507 has a marginally sub-threshold preference ($\ln(\mathcal{B}) = 4.9$). These measurements of $\dot{\nu}$ along with the inferred braking index for each pulsar are compared with those from PSRCAT in Table 2. The sign of the braking indices depends on whether the inferred value of $\dot{\nu}$ is positive or negative. None of our measurements of $\dot{\nu}$ and n are consistent with previously published values. Given each of the pulsars with previous $\dot{\nu}$ measurements have undergone glitches, the difference in results may be due to the accumulated changes in pulsar rotation between measurements or yet to be reported glitches. No glitches have been reported to date in the pulsars that do not have $\dot{\nu}$ values listed in PSRCAT. While the inferred braking indices are all much larger than the canonical $n = 3$

expected from magnetic dipole radiation, they are consistent with values reported for other young pulsars. It has been speculated these large braking indices may be due to the effects of unmodelled recovery from glitches prior to the start of timing observations (Johnston & Galloway 1999). Alternatively, our timing noise model may be incomplete, giving rise to the preference for the PLRN+F2 model. For instance, PSR J0738–4042 may be affected by torque variations initially induced after a profile change in 2005, proposed to be evidence for an interaction with an asteroid (Brook et al. 2014), while PSR J1001–5507 is known to exhibit discrete spin-down state switching (Chukwude & Buchner 2012). Neither phenomenon is included in the timing models for these pulsars, and are therefore likely causes of these pulsars’ strong preference for the PLRN+F2 model.

4.3 Red timing noise properties

We assessed the presence of red noise in our pulsars using the Bayes factor found from comparing the PLRN model against the WTN model as a detection statistic, where $\ln(\mathcal{B}_{R/W}) > 5$ is a strong detection. Pulsars for which we obtain Bayes factors of $3 < \ln(\mathcal{B}_{R/W}) < 5$ are categorized as ‘probable detections’ since the PLRN model is favoured, but is subject to an increased false positive rate. Those that have Bayes factors in the range $1 < \ln(\mathcal{B}_{R/W}) < 3$ marginally favour a red noise model, but lack the statistical confidence to be distinguishable from the WTN model.

Out of the 300 pulsars analysed, we find 110 strongly favour the PLRN model and 6 that fall into the probable detection category. None of the pulsars in our sample favour the PL+FC model. We find the magnetar PSR J1622–4950 to have the largest red noise amplitude at 1 yr of $\log_{10}(A) = -4.9^{+0.6}_{-0.4}$, with a spectral index $\beta = 7.3^{+3.4}_{-3.6}$. This result should be taken with caution as we do not account for changes in the pulse profile or variations in $\dot{\nu}$ due to short-term changes in magnetic torque that are observed in magnetars (e.g. Camilo et al. 2018). Excluding magnetars, PSR J0835–4510 (the Vela pulsar) has the largest red noise amplitude of any non-recycled pulsar in our data set, with $\log_{10}(A) = -8.2 \pm 0.2$ and a steep spectral index of $\beta = 8.6 \pm 0.9$. This spectral index is different to the value measured by Shannon et al. (2016) using 21 years of Vela timing, which may be caused by the occurrence of additional glitches that have recovered since the end of their data set.

We find that three millisecond pulsars favour the PLRN model:

¹⁰ This is the psrcat version from which many of initial ephemerides were drawn from.

¹¹ github.com/Molonglo/TimingDataRelease1/

Table 2. Maximum likelihood posterior measurements of $\dot{\nu}$ and n compared with reported values in the literature. Values in parentheses indicate the 1σ uncertainties in the last digits, while the errors in our measurements indicate the 95 percent confidence intervals. Only PSR J0738–4042 strongly favours the PLRN+F2 model over the standard PLRN model.

PSR	$\ln(\mathcal{B})$	$\dot{\nu}$ (10^{-24}s^{-3})	$\dot{\nu}_{\text{lit}}$ (10^{-24}s^{-3})	n	n_{lit}	τ_c Myr	Known to glitch?
J0659+1414	1.5	$1.1^{+1.1}_{-0.5}$	0.764(4)	$21.1^{+2.7}_{-1.2}$	14.44(8)	0.111	Y
J0729–1836	3.6	$-2.4^{+2.3}_{-1.9}$	0.376(15)	$-897.1^{+10.3}_{-5.2}$	139(5)	0.426	Y
J0738–4042	5.4	-3.5 ± 1.2	–	$-96227.0^{+1.8}_{-2.2}$	–	4.32	N
J0942–5552	1.6	$8.1^{+4.2}_{-4.3}$	–	$4591.4^{+3.1}_{-3.5}$	–	0.461	N
J1001–5507	4.9	$1.8^{+0.8}_{-1.5}$	–	$1960.1^{+1.4}_{-4.1}$	–	0.441	N
J1359–6038	4.1	$-3.4^{+3.3}_{-1.1}$	–	$-176.9^{+4.6}_{-1.4}$	–	0.319	N
J1413–6307	1.1	$-4.2^{+3.5}_{-11.2}$	–	$-4606.1^{+2.4}_{-16.5}$	–	0.842	N
J1709–4429	1.0	$106.4^{+45.1}_{-47.3}$	173.1(7)	$13.3^{+0.8}_{-0.3}$	21.35(8)	0.0175	Y
J1909+1102	3.2	$1.1^{+0.7}_{-1.0}$	$-2.02(4)$	$3466.9^{+3.9}_{-5.1}$	$-6615(131)$	1.7	Y

PSR J0437–4715, PSR J2145–0750 and PSR J2241–5236. While red noise due to rotational instabilities is known to be present in millisecond pulsars, high precision timing has shown that variations in pulsar DM can mimic timing noise in observations at single frequencies (e.g., [Lentati et al. 2016](#)). Accounting for DM variations requires observing systems that use either wide-band receivers or are capable of observing at multiple frequencies. Due to the limited bandwidth of UTMOST, there is a covariance between DM variations and achromatic timing noise. Hence it is not possible for us to attribute the red noise we observe in millisecond pulsars to rotational irregularities. Unaccounted instrumental artefacts may also contribute to the red noise in these pulsars ([Jankowski et al. 2019](#)).

The lack of multi-band observations also means we cannot infer the contribution of DM variations to the red noise in the non-recycled pulsars. However, [Petroff et al. \(2013\)](#) found only 11 pulsars out of a sample of 160 non-recycled pulsars showed significant changes in DM with time (only setting upper-limits on the remaining 149), while [Shannon et al. \(2016\)](#) showed the Vela pulsar’s DM variations have a sub-dominant contribution to its overall red noise. Hence, any extra red noise induced by DM variations in our non-recycled pulsar sample would be negligible. Additionally, we find no correlation between red noise parameters and DM.

The full list of the maximum likelihood posterior values and associated 95 percent confidence intervals on the red noise parameters are presented in Appendix B.

4.4 Pulsar glitch reanalysis

So far we have observed twelve glitches in eight pulsars, nine of which have been previously reported.¹² The timing residuals for the six pulsars prior to adding glitch corrections are depicted in Fig. 3. Cusp-like features in the residuals are the result of large glitches. Note that separate ephemeris and ToA files for PSRs J0835–4510, J1257–1027, J1452–6036 and J1703–4851 that include post-glitch observations and corrections can be found in the online repository¹³. The extended data sets for these pulsars are used only for the glitch analyses, and are not included in our red

noise study. Currently pulsars that have undergone a glitch are manually identified in the UTMOST data by searching for glitch-like events in the timing residuals ‘by eye’. This method can be prone to error, with small glitches being glossed over when investigating pulsars that exhibit strong red noise. An automated glitch detection pipeline would be a useful development to search for previously unnoticed glitches in past observations and for near-real time glitch detection.

PSR J0835–4510

There are three reported glitches in PSR J0835–4510 that we have observed with UTMOST ([Jankowski et al. 2015a](#); [Palfreyman et al. 2016](#); [Palfreyman et al. 2018](#); [Sarkissian et al. 2019](#); [Kerr 2019](#)). The first is reported to have occurred on MJD 56922 ± 3 , with a small glitch amplitude of $\Delta\nu_g/\nu = 0.4 \times 10^{-9}$. Our reanalysis returns only upper limits on the change in ν , but does recover $\Delta\dot{\nu}_g = 21.5^{+0.6}_{-1.4} \times 10^{-3}$. However, performing model comparison returns a log Bayes factor of $\ln(\mathcal{B}) = -48.0$, indicating a red noise model without a glitch at this epoch is strongly preferred for this event.

For the second glitch, which was observed in real-time by [Palfreyman et al. \(2018\)](#) at MJD 57734.484991(29), we obtain a glitch amplitude that is similar in magnitude to the published value, while our inferred change in the spin-down of the pulsar is ~ 30 percent smaller than the previously reported value. This is likely due to our analysis incorporating simultaneous modelling of the glitch and timing noise parameters. Including the short-term recovery found by [Sarkissian et al. \(2017\)](#), we find evidence for additional recovery of $\Delta\nu_d = 4.2^{+0.6}_{-0.3}$ nHz over $12.7^{+3.0}_{-1.2}$ days.

The third glitch occurred during observations by the Hawksbury radio observatory ([Sarkissian et al. 2019](#)) and the *Fermi* gamma-ray observatory at MJD 58515.5929(5) ([Kerr 2019](#)). Our recovered glitch amplitude is similar in size to the previously reported values, and is typical of other large Vela glitches ($\Delta\nu_g/\nu \sim 1000$). We also find a small exponential recovery ($Q = 0.005$) occurred over 11.0 ± 1.2 days. We are unable to test whether this glitch underwent any short-term recovery similar to the previous one as our first post-glitch observation was ~ 9 days after the glitch occurred.

In addition to the three glitches we analyse here, a large glitch occurred on MJD 56555.871 ([Buchner 2013](#); [Shannon et al. 2016](#)),

¹² Seven of these glitches have been added to the Jodrell Bank glitch catalogue ([Espinoza et al. 2011](#)): www.jb.man.ac.uk/pulsar/glitches.html

¹³ github.com/Molonglo/TimingDataRelease/

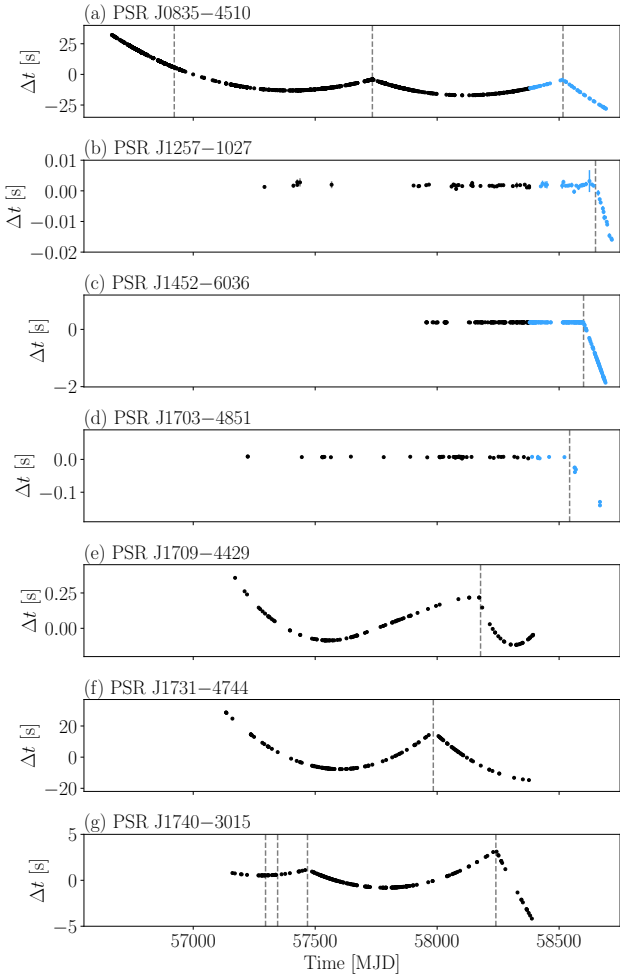


Figure 3. Timing residuals for the four glitched pulsars after fitting for ν and $\dot{\nu}$. The epochs of the reported glitches are indicated by the dashed vertical lines. Light blue points in (a), (b), (c) and (d) indicate ToAs that are not used in the red noise analysis.

prior to the start of our data set. While we cannot constrain the permanent changes in ν and $\dot{\nu}$, we can perform parameter estimation on the recovery parameters in the presence of red noise. We obtain a change in spin frequency of $\Delta\nu_d/\nu = 1591_{-322}^{+170}$, which decays over $\tau_d = 923_{-152}^{+88}$ days. Our measured $\Delta\nu_d/\nu$ is inconsistent with the value inferred by Shannon et al. (2016), but they only have observations up to 116 days after the glitch occurred. Hence any further decay in $\Delta\nu_g$ beyond the end of their data set will have been missed. When compared against the pure PLRN model, the resulting $\ln(\mathcal{B}) = 65.5$ strongly favours the red noise plus glitch recovery model. This confirms that long-term recovery from glitches prior to the start of timing observations can affect the recovered timing parameters.

PSR J1257–1027

This glitch is the first to ever be reported in this pulsar. It is well described by a small permanent change in the pulsar spin ($\Delta\nu_g/\nu = 3.20_{-0.57}^{+0.16} \times 10^{-9}$) with no evidence for recovery. Including a change in the pulsar’s spin-down frequency in our parameter estimation returned only an upper limit of $\Delta\dot{\nu} \lesssim 268 \times 10^{-3}$.

Additional observations over longer post-glitch timescales are required for further constraints to be placed on changes in $\dot{\nu}$.

PSR J1452–6036

We discovered a glitch with an amplitude of $\Delta\nu_g/\nu = 270.7_{-0.4}^{+0.3} \times 10^{-9}$ that occurred in PSR J1452–6036 on MJD 58600.29(5). This is the second glitch seen in this pulsar to date and is almost a factor of 10 larger than the glitch observed on MJD 55055.22(4) by Yu et al. (2013). Performing model selection we find a change in spin-down is weakly disfavoured ($\ln(\mathcal{B}) = 4.2$), hence we can only set an upper limit on $\Delta\dot{\nu}_g/\dot{\nu}$ of $\lesssim 16 \times 10^{-3}$ at the 95 percent confidence level. In addition, we find no evidence for an exponential recovery after this glitch. This could be due to a lack of vortex re-pinning following this glitch, or the recovery having occurred on a timescale too short to be resolved with our current observation cadence (~ 3.3 days between t_g and the first post-glitch observation). Alternatively, the recovery timescale may be significantly longer than our current post-glitch data span.

PSR J1703–4851

The glitch we observed on MJD 58543.1(3) is the first to ever be reported in this pulsar. We recover a moderate change in the pulsar spin of $\Delta\nu_g/\nu = 19.0_{-0.7}^{+1.0} \times 10^{-9}$ and a relatively large change in the spin-down of $\Delta\dot{\nu}_g/\dot{\nu} = 292_{-53}^{+38} \times 10^{-3}$. We find a recovery model is disfavoured for this glitch. While this pulsar is known to undergo emission state switching (Wang et al. 2007) we have only four post-glitch observations to date, hence we are currently unable to provide any link between the glitch and state switching. The lack of post-glitch observations may also explain why the recovery model is disfavoured, as long-term glitch recoveries require extended observations to detect.

PSR J1709–4429

This glitch is the fourth and smallest glitch observed to date in PSR J1709–4429. The glitch amplitude we recover ($\Delta\nu_g/\nu = 54.6 \pm 1.0 \times 10^{-9}$) is consistent with the previously reported value (Lower et al. 2018), but the change in spin-down frequency was overestimated by a factor of ~ 7 . This is likely due to $\Delta\dot{\nu}$ being covariant with the glitch recovery, which was not fit for in Lower et al. (2018). We find the change-in-spin period due to this glitch almost completely recovers ($Q = 0.995$) in $99.1_{-9.6}^{+11.2}$ days.

PSR J1731–4744

With an amplitude of $\Delta\nu_g/\nu = 3148 \pm 3 \times 10^{-9}$, this is the largest glitch contained within our presented data set, and the largest observed in this pulsar to date (Espinoza et al. 2011). Previous glitches have shown evidence for linear recoveries (Yu et al. 2013), but we find no evidence for any spin recovery from this glitch.

PSR J1740–3015

Four previously reported glitches have occurred within our timing measurements of PSR J1740–3015 (Jankowski et al. 2015b, 2016; Espinoza et al. 2011; Liu et al. 2019). We obtain a small amplitude of $\Delta\nu_g/\nu = 0.122_{-0.081}^{+0.086} \times 10^{-9}$ and comparatively large change in spin-down ($\Delta\dot{\nu}_g = 82.2_{-8.5}^{+8.8} \times 10^{-3}$) associated with the first glitch. For the second glitch (MJD 57346.0(0.6)), we are only able to set

Table 3. Maximum likelihood posterior values from the glitch parameter posterior distributions and associated 95 percent confidence intervals compared with previously reported measurements. Values in parentheses represent the $1\text{-}\sigma$ uncertainties on the last digit.

PSR	t_g MJD	$\Delta\nu_g/\nu$ $\times 10^{-9}$	$\Delta\dot{\nu}_g/\dot{\nu}$ $\times 10^{-3}$	τ_d days	Q	$(\Delta\nu_g/\nu)_{\text{lit}}$ $\times 10^{-9}$	$(\Delta\dot{\nu}_g/\dot{\nu})_{\text{lit}}$ $\times 10^{-3}$	Ref
J0835–4510	56922(3)	$\lesssim 0.2$	$21.5^{+0.6}_{-1.4}$	–	–	0.4	0.1	1, 2
J0835–4510	57734.484991(29)	$*1448.8^{+0.9}_{-0.8}$	$7.33^{+0.13}_{-0.11}$	$12.7^{+3.0}_{-1.2}$	$*0.011$	1431.24(7)	9.20(83)	3, 4
J0835–4510	58515.5929(5)	$2501.2^{+2.6}_{-3.2}$	$8.69^{+0.28}_{-0.25}$	11.0 ± 1.2	0.005	2491.1(5)	–	5, 6
J1257–1027	58649.3(6)	$3.20^{+0.16}_{-0.57}$	$\lesssim 286$	–	–	–	–	This work
J1452–6036	58600.29(5)	$270.7^{+0.3}_{-0.4}$	$\lesssim 16$	–	–	–	–	This work
J1703–4851	58543.1(3)	$19.0^{+1.0}_{-0.7}$	292^{+38}_{-53}	–	–	–	–	This work
J1709–4429	58178(6)	54.6 ± 1.0	$1.06^{+0.36}_{-0.43}$	$99.1^{+11.3}_{-9.6}$	0.995	52.4(1)	7.30(12)	7
J1731–4744	57984(20)	$3149.5^{+0.5}_{-0.4}$	$1.2^{+0.7}_{-1.1}$	–	–	3147.7(1)	–	8
J1740–3015	57296.5(9)	$0.122^{+0.086}_{-0.081}$	$82.2^{+8.8}_{-8.5}$	–	–	1.30(4)	< 0.66	9, 10
J1740–3015	57346.0(6)	$\lesssim 0.019$	$111.1^{+13.6}_{-8.4}$	–	–	1.94(2)	< 0.07	11
J1740–3015	57468.59(40)	$237.7^{+13.2}_{-9.3}$	$1.71^{+3.24}_{-1.54}$	430^{+91}_{-101}	0.025	229(2)	2.19(4)	11, 10
J1740–3015	58240.781(5)	$842.3^{+7.1}_{-5.6}$	$74.0^{+10.0}_{-13.2}$	–	–	837.88(28)	1.63(14)	12, 10

References indicated in the last column are (1) Jankowski et al. (2015a); (2) Palfreyman et al. (2016); (3) Sarkissian et al. (2017); (4) Palfreyman et al. (2018); (5) Sarkissian et al. (2019); (6) Kerr (2019); (7) Lower et al. (2018); (8) Jankowski et al. (2017); (9) Jankowski et al. (2015b); (10) Espinoza et al. (2011); (11) Jankowski et al. (2016); (12) Liu et al. (2019). *Includes a short-term $\Delta\nu_d = 129(8)$ nHz recovery over 0.96(17) days (Sarkissian et al. 2017).

an upper-limit on the instantaneous change in pulsar spin-frequency. Performing model comparison, we find all models that include the second glitch are strongly disfavoured, suggesting the properties of this glitch are covariant with our red timing noise model. Our analysis of the third glitch recovers a change in spin-frequency that is largely consistent with previously reported values, with a small recovery ($Q = 0.035$) over $430^{+91.1}_{-100.9}$ days. The fourth glitch was discovered in observations of the pulsar at Jodrell Bank (Shaw et al. 2018, private communication, Espinoza et al. 2011). It was also seen by the Shanghai Tian Ma Radio Telescope (Liu et al. 2019). We find no evidence for spin recovery after this latest glitch. However, the large change in spin-down we recover may be evidence of longer-term recovery, as these two effects are strongly covariant while the pulsar remains in the recovery phase.

4.4.1 Glitch-like events in PSR J1825–0935

Also known as PSR B1822–09, this pulsar has been reported to exhibit timing events, sometimes referred to as ‘slow glitches’ (Zou et al. 2004; Shabanova 2007). These events are predominantly characterized by a sharp change in the spin-down of the pulsar, which leads to the pulsar spinning up over the course of a few days. This change in spin-down decays exponentially over timescales of days to months. PSR J1825–0935 is also known to switch between two emission states: a ‘B-mode’ where an extra precursor component adjacent to the main pulse is visible, and a ‘Q-mode’, where precursor emission is suppressed and emission from an interpulse component is brightest (Fowler et al. 1981; Morris et al. 1981; Gil et al. 1994). Lyne et al. (2010) showed this switching between these two emission modes is correlated with changes in the spin-down rate, concluding the apparent ‘slow glitches’ are not related to the glitch phenomena, but are instead a result of the pulsar spending more time in one emission/spin-down state versus the other.

The upper panel of Fig. 4 shows the timing residuals for PSR

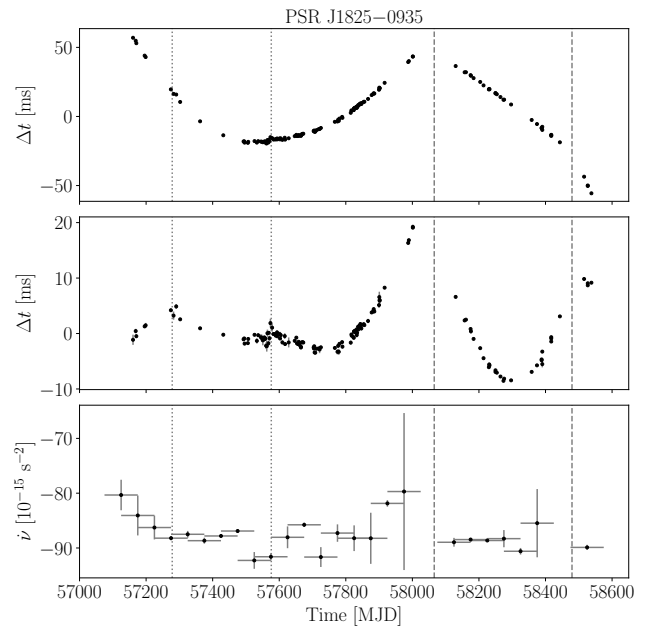


Figure 4. Post-fit timing residuals for PSR J1825–0935. Top plot shows the residuals after removing a fit for only ν and $\dot{\nu}$, while the middle plot includes a fit for $\dot{\nu}$. Bottom plot shows changes in the spin-down frequency over time as determined via fitting $\dot{\nu}$ over ~ 50 day segments (error bars indicate the 1-sigma error). Vertical dashed lines in all three panels correspond to the approximate epochs of the largest events; dotted lines indicate the two smaller events.

J1825–0935 after subtracting a fit for ν and $\dot{\nu}$. Two glitch-like events are found to have occurred during observing gaps centred at

Table 4. Recovered glitch parameters for the events in PSR J1825–0935.

No.	t_g (MJD)	$\Delta\nu_g/\nu$ ($\times 10^{-9}$)	$\Delta\dot{\nu}_g/\dot{\nu}$ ($\times 10^{-3}$)
1	57278.5(41)	$\lesssim 0.9$	$-1.3^{+2.7}_{-2.0}$
2	57576.1(26)	$\lesssim 0.3$	$-0.9^{+1.1}_{-2.0}$
3	58065.7(3)	$5.2^{+1.7}_{-0.5}$	$-1.1^{+1.7}_{-2.4}$
4	58486.2(9)	$7.6^{+4.5}_{-3.3}$	$14.6^{+37.3}_{-20.0}$

MJD 58065(64) and MJD 58484.8(9)¹⁴. Including a fit for $\ddot{\nu}$ in our timing model reveals two additional events with lower amplitudes that occurred at MJD 57278.5(41) and MJD 57576.1(26). Modelling these four events as standard pulsar glitches, we perform parameter estimation using TEMPO_NEST to fit for step changes in ν and $\dot{\nu}$. The recovered glitch parameters are presented in Table 4. The first two events are only consistent with upper limits on an instantaneous changes in ν , while the changes in $\dot{\nu}$ both peak at negative values. Changes in $\Delta\dot{\nu}_g$ for all four events are consistent with zero at the 95 percent confidence interval. However, the standard glitch model we employ does not sufficiently describe the true nature of these events. By performing model selection, we find a PLRN model with no glitches is preferred over any glitch+PLRN model, with a $\ln(\mathcal{B}) = 14$ when comparing a PLRN-only model to PLRN+4 glitches and $\ln(\mathcal{B}) = 7.8$ in favour of the PLRN-only model versus a fit to only the two large events. Subtracting off the purely red noise model the post-fit residuals are still dominated by the two larger glitch-like events, implying that at least these two events are not related to the pulsar’s red noise.

The small variations in $\dot{\nu}$ in the bottom panel of Fig. 4 at the time of each event are more in line with conventional pulsar glitches as opposed to slow glitches, although the lack of coverage around the more recent large amplitude events means we may have insufficient resolution to detect any rapid changes in spin-down. The mode-changing behaviour and glitch-like events of PSR J1825–0935 demand further investigation, as high-cadence coverage of these events, and any that are discovered in other mode-changing pulsars, may allow us to probe the internal dynamics of these neutron stars.

5 DISCUSSION

5.1 Quantifying timing noise strength

While a complete characterisation of pulsar timing noise is yet to be achieved, previous work usually followed one of two approaches. The first involves applying a cubic polynomial to fit for $\ddot{\nu}$ to assess the effects of timing noise. The second uses the root-mean-square (RMS) of the residuals after subtracting a quadratic polynomial, which corresponds to a fit for only ν and $\dot{\nu}$.

Studies undertaken by Urama et al. (2006) and Chukwude (2007) use measurements of $\ddot{\nu}$ to directly infer the strength of the timing noise in their data sets, in addition to searching for correlations with other pulsar parameters. Other users of $\ddot{\nu}$ measurements include work by Arzoumanian et al. (1994) through the use of a model-dependent parameter

$$\Delta_8 = \log\left(\frac{|\ddot{\nu}|}{6\nu} T_8^3\right), \quad (12)$$

¹⁴ The last event is listed as a glitch in the Jodrell Bank glitch catalogue at MJD 58486.2(9).

where $\ddot{\nu}$ is measured over a total (but arbitrary) observation time span of $T_8 = 10^8$ s. A two-sample variance parameter σ_z is used in Matsakis et al. (1997) to describe pulsar rotational stability

$$\sigma_z = \frac{1}{2\sqrt{5}} \left[\frac{\sigma_{\ddot{\nu}}(T)}{\nu} \right] T^2, \quad (13)$$

where $\sigma_{\ddot{\nu}}(T)$ is the RMS of the $\ddot{\nu}$ fit over the observing span T . Shannon & Cordes (2010) note that the Δ_8 method is highly model-dependent since the measured $\ddot{\nu}$ will usually increase on longer timescales, requiring additional time dependent scaling to properly compare values of $\ddot{\nu}$ and Δ_8 . They also state methods based around measurements of $\ddot{\nu}$ (such as σ_z) will often underestimate the amount of timing noise as they neglect contributions from higher-order frequency derivatives.

A method proposed by Cordes & Helfand (1980) assesses the RMS of the total timing noise after conducting a second order fit

$$\sigma_{\mathcal{R},2}^2(T) = \frac{1}{N} \sum_i^N \mathcal{R}(t_i)^2, \quad (14)$$

where \mathcal{R} refers to the timing residuals and N is the number of ToAs. This can be further broken down into red and white components

$$\sigma_{\mathcal{R},2}^2(T) = \sigma_{\text{TN},2}^2(T) + \sigma_{\text{W}}^2(T). \quad (15)$$

It is assumed the RMS is usually dominated by $\sigma_{\text{TN},2}^2$ in slow ($P \sim 1$ s) pulsars. The timing noise strength is then estimated via an activity parameter that describes the scaling of $\sigma_{\text{TN},2}$ with respect to PSR J0534+2200 (the Crab pulsar) by

$$A = \log \left[\frac{\sigma_{\text{TN},2}(T)}{\sigma_{\text{TN},2}(T)_{\text{Crab}}} \right]. \quad (16)$$

This method assumes the timing noise scales in the same way as the Crab pulsar. Dewey & Cordes (1989), and later Shannon & Cordes (2010) built upon this method by assessing how timing noise varies across the population by examining a scaling relationship between timing noise strength and ν , $\dot{\nu}$ and the observation time span T (in years) as

$$\hat{\sigma}_{\text{TN},2} = C_2 \nu^a |\dot{\nu}|^b T^\gamma. \quad (17)$$

Here, the fitting factors C_2 , a , b and γ are measured from the total pulsar population using fits based on maximum likelihood statistics.

We note these methods do not attempt to model the timing noise directly. Instead, they assume the RMS of the residuals accurately describes the timing noise strength. This neglects covariances between intrinsic pulsar properties and red noise, which can result in contaminated residuals as some pulsar properties may be over- or under-fit. This is not an issue for modern Bayesian methods that model both deterministic and stochastic properties simultaneously.

The method we use for assessing timing noise strength was developed in parallel with Parthasarathy et al. (2019), in which timing noise strength is inferred from the red noise amplitude and spectral index, obtained via parameter estimation with TEMPO_NEST, and the observation span as

$$\sigma_{\text{RN}}^2 = A^2 T^{\beta-1}. \quad (18)$$

Using this metric, we find the magnetar PSR J1622–4950 has the strongest timing noise in our sample. However, as stated earlier the torque variations due to the magnetar’s decaying magnetic field, rather than spin noise, are expected to dominate the observed red noise. In addition, Shannon & Cordes (2010) argued that timing noise in magnetars is statistically different to that in millisecond and non-recycled pulsars. Given the red noise we observe in both the millisecond pulsars and PSR J1622–4950 can be explained via

Table 5. Frequentist (r_p) and Bayesian (ρ) correlations between pulsar properties and red noise strength, using only strong red noise detections (D) and including lower confidence detections (D + PD). Errors represent the 95 percent confidence intervals.

	D		D + PD	
	r_p	ρ	r_p	ρ
ν	0.13	$0.18^{+0.29}_{-0.26}$	0.16	$-0.18^{+0.33}_{-0.25}$
$\dot{\nu}$	0.45	$0.47^{+0.29}_{-0.20}$	0.46	$0.47^{+0.27}_{-0.20}$
\dot{P}	0.49	$0.51^{+0.28}_{-0.18}$	0.49	$0.48^{+0.24}_{-0.21}$
τ	-0.51	$-0.51^{+0.19}_{-0.25}$	-0.51	$-0.53^{+0.17}_{-0.26}$
B_{surf}	0.37	$0.39^{+0.30}_{-0.22}$	0.37	$0.38^{+0.28}_{-0.22}$
\dot{E}	0.39	$0.41^{+0.30}_{-0.21}$	0.41	$0.42^{+0.29}_{-0.20}$

processes other than rotational irregularities, we restrict our analysis to the 280 non-recycled pulsars in our sample, 112 of which strongly favour the PLRN model.

5.2 Correlations with individual pulsar properties

A number of pulsar properties can be inferred from their spin and spin-down. These include the characteristic age (τ_c), surface dipole magnetic field strength (B_{surf}) and the rotational kinetic energy loss over time (\dot{E}). Simplified approximations to these properties, along with the pulse period derivative (\dot{P}), can be expressed in terms of the spin and spin-down frequencies, as follows

$$\begin{aligned}
 \dot{P} &\propto \nu^{-2} |\dot{\nu}| \\
 \tau_c &\propto \nu |\dot{\nu}|^{-1} \\
 B_{\text{surf}} &\propto \nu^{-3/2} |\dot{\nu}|^{1/2} \\
 \dot{E} &\propto \nu |\dot{\nu}|.
 \end{aligned} \tag{19}$$

Similar to previous work on pulsar timing noise, we examine whether correlations exist between the measured red noise strength and these pulsar properties, in addition to the spin and spin-down on their own. Assuming timing noise strength scales with spin and spin-down frequencies in a similar fashion to Equation 17, we compared the inferred strength against a predictive metric

$$\chi_{\text{RN}} \propto \nu^a |\dot{\nu}|^b, \tag{20}$$

where the values of a and b can be set to the approximate pulsar properties we are comparing.

From a frequentist perspective, the amount of correlation between σ_{RN} and χ_{RN} can be quantified via the Pearson correlation coefficient

$$r_p = \frac{\sum_{i=1}^N (\sigma_{\text{RN},i} - \mu_\sigma)(\chi_{\text{RN},i} - \mu_\chi)}{[\sum_{i=1}^N (\sigma_{\text{RN},i} - \mu_\sigma)^2 \sum_{i=1}^N (\chi_{\text{RN},i} - \mu_\chi)^2]^{1/2}}, \tag{21}$$

where $\mu_\sigma = \frac{1}{N} \sum_{i=1}^N \sigma_{\text{RN},i}$ is the mean of the σ_{RN} values, and μ_χ is the mean of χ_{RN} . However, this approach does not take into account potential covariances between the means of $\sigma_{\text{RN},i}$ and $\nu^a |\dot{\nu}|^b$, or scatter in the measurements. It is also not robust against the influence of outliers in the data set.

An alternative approach involves assuming the red noise measurements and values generated from equation 20 are correlated samples drawn from an underlying bivariate Gaussian distribution, the shape of which is best described by the set of hyper-parameters

$\{\mu_\sigma, \mu_\chi, \sigma_\sigma, \sigma_\chi, \rho\}$ as

$$\begin{aligned}
 \mathcal{N}_2(\sigma_{\text{RN}}, \chi_{\text{RN}}) &= \frac{1}{2\pi\sigma_\sigma\sigma_\chi\sqrt{1-\rho^2}} \exp\left[\frac{-1}{2(1-\rho^2)}\right. \\
 &\quad \left. \times \left(\frac{\sigma_{\text{RN}}^2}{\sigma_\sigma^2} + \frac{\chi_{\text{RN}}^2}{\sigma_\chi^2} - \frac{2\rho\sigma_{\text{RN}}\chi_{\text{RN}}}{\sigma_\sigma\sigma_\chi}\right)\right].
 \end{aligned} \tag{22}$$

Here, $\mu_\sigma, \sigma_\sigma$ are the mean and variance of the distribution in the σ_{RN} direction, and μ_χ, σ_χ represent the mean and width in the χ_{RN} direction. The parameter ρ indicates the direction in which the bivariate Gaussian is rotated and provides an estimate for the level of correlation between σ_{RN} and χ_{RN} . For simplicity, we express the bivariate Gaussian as $\mathcal{N}_2(\sigma_{\text{RN}}, \chi_{\text{RN}}) = \theta^T \mathbf{C}^{-1} \theta$, where \mathbf{C} is the covariance matrix

$$\mathbf{C} = \begin{bmatrix} \sigma_\sigma^2 & \rho\sigma_\sigma\sigma_\chi \\ \rho\sigma_\sigma\sigma_\chi & \sigma_\chi^2 \end{bmatrix}, \tag{23}$$

and $\theta = (\sigma_{\text{RN}} - \mu_\sigma, \chi_{\text{RN}} - \mu_\chi)$. We can then write the likelihood function from which our samples are drawn from as

$$\mathcal{L}(\theta|\mathbf{C}) = \frac{1}{2\pi\sqrt{|\mathbf{C}|}} \prod_{i=1}^N \exp\left[\frac{-1}{2}\theta_i^T \mathbf{C}^{-1} \theta_i\right], \tag{24}$$

where $|\mathbf{C}| = \sigma_\sigma^2 \sigma_\chi^2 (1 - \rho^2)$. We use the *BILBY* software library (Ashton et al. 2019b) and *PyMULTINEST* (Buchner et al. 2014), a Python wrapper for the *MULTINEST* algorithm, to sample the hyper-parameter posterior distributions using the 112 non-recycled pulsars that strongly favour the PLRN model, ignoring those that are consistent with the WTN model. The resulting Frequentist and Bayesian correlation coefficients for pulsars with strong evidence for red noise (D; $\ln(\mathcal{B}) > 5$) and when including those with less confident evidence (D + PD; $3 < \ln(\mathcal{B}) < 5$) are presented in Table 5.

We find the strongest correlations exist with \dot{P} and $\dot{\nu}$, in addition to a similar anti-correlation with characteristic age. These correlations are smaller than those from the σ_z analysis performed by Hobbs et al. (2010), who presented an analysis of the ongoing timing campaign of a large sample of pulsars at the Jodrell Bank Observatory ($N = 366$, $T_{\text{mean}} \sim 19$ yr), but are similar to those from Namkham et al. (2019) who assessed the timing noise of 129 ‘middle-aged’ ($\tau_c \sim 1$ Myr) pulsars observed by the Parkes radio telescope over ~ 4 yr using the σ_z metric. We find pulsar spin-frequency has effectively no correlation with timing noise, but the weak correlation of 0.3 from Hobbs et al. (2010) does overlap with the 95 percent confidence region of our Bayesian correlation parameter for the pulsars that strongly prefer the PLRN model. These differences are to be expected as Hobbs et al. (2010) included both millisecond and partially-recycled pulsars when calculating their correlation coefficients, while we are limited to non-recycled pulsars.

5.3 Scaling relation fitting and hyper-parameter estimation

To see how the timing noise strength varies independently of specific pulsar properties, we build upon previous work by Dewey & Cordes (1989) and (Shannon & Cordes 2010) for finding a scaling relation that maps timing noise strength to a scaling of pulsar ν and $\dot{\nu}$, and observing timescale T . We rewrite their scaling relation (Equation 20) as

$$\chi_{\text{RN}} = \xi \nu^a |\dot{\nu}|^b T^\gamma, \tag{25}$$

where Shannon & Cordes (2010) use the symbol C_2 in place of ξ to represent the linear scaling factor. Unlike in Section 5.2, a and b

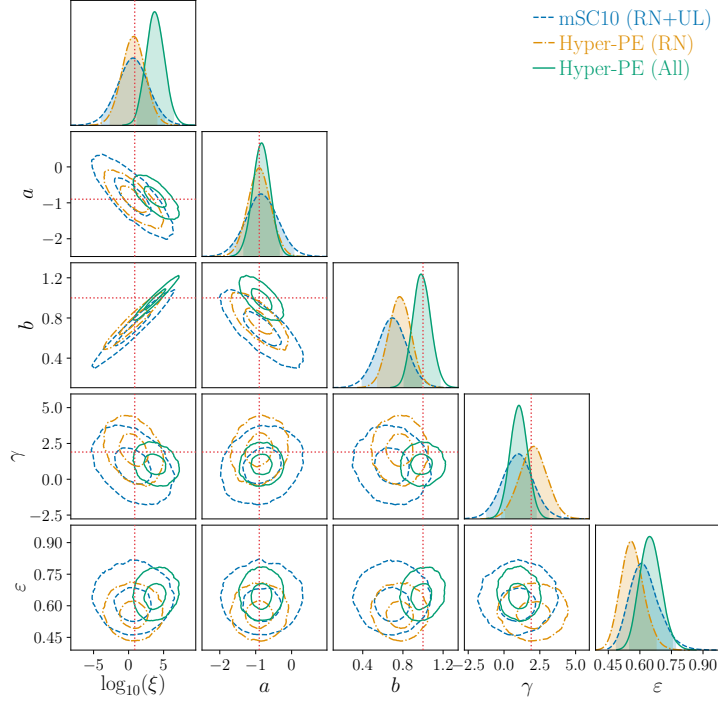


Figure 5. One- and two-dimensional posterior distributions for the scaling parameters across the non-recycled pulsar population. Contours in the two-dimensional posteriors indicate the 50 and 95 percent confidence regions. Shading in the one-dimensional posteriors covers the 95 percent confidence intervals. The red dotted lines indicate the non-recycled pulsar maximum likelihood values from [Shannon & Cordes \(2010\)](#).

are not set to fixed values to approximate certain pulsar properties. Instead we allow them to be free parameters with uniformly sampled priors ($-10 < \pi(a, b) < 10$).

[Shannon & Cordes \(2010\)](#) define the joint likelihood function

$$\mathcal{L}(\sigma_{\text{RN}}, \sigma_{\text{UL}} | \chi_{\text{RN}}, \varepsilon) = \mathcal{L}(\sigma_{\text{RN}} | \chi_{\text{RN}}, \varepsilon) \times \mathcal{L}(\sigma_{\text{UL}} | \chi_{\text{RN}}, \varepsilon), \quad (26)$$

which is comprised of a standard Gaussian likelihood with an additional hyper-parameter ε^2 to describe the scatter in the measured red noise strength in the pulsar sample, which may be attributed to variations in the amount of turbulence in their superfluid interiors ([Melatos & Link 2014](#)), and an upper-limit likelihood. The likelihood functions contributing to Equation 26 are given by

$$\mathcal{L}(\sigma_{\text{RN}} | \chi_{\text{RN}}, \varepsilon) = \prod_i^N \frac{1}{\sqrt{2\pi\varepsilon^2}} \exp \left[-\frac{(\sigma_{\text{RN},i} - \chi_{\text{RN},i})^2}{2\varepsilon^2} \right], \quad (27)$$

and

$$\mathcal{L}(\sigma_{\text{UL}} | \chi_{\text{RN}}, \varepsilon) = \prod_j^N \left[1 - \frac{1}{2} \operatorname{erfc} \left[-\frac{(\sigma_{\text{UL},j} - \mu_{\text{RN},j})}{\varepsilon\sqrt{2}} \right] \right], \quad (28)$$

where σ_{UL} is the ‘upper limit’ on the red noise strength and erfc is the complementary error function. We use this likelihood to calculate posterior distributions for the scaling hyper-parameters as follows

$$p(\chi_{\text{RN}}, \varepsilon | \sigma_{\text{RN}}, \sigma_{\text{UL}}) \propto \mathcal{L}(\sigma_{\text{RN}}, \sigma_{\text{UL}} | \chi_{\text{RN}}, \varepsilon) \pi(\chi_{\text{RN}}, \varepsilon). \quad (29)$$

This modified version of the [Shannon & Cordes \(2010\)](#) formalism (mSC10 hereafter) requires making two key assumptions: scatter in the maximum likelihood posterior values of σ_{RN} due to measurement uncertainties are either negligible or absorbed by ε , and the upper limit likelihood holds true for the pulsars with only a marginal preference (i.e. $1 < \ln(\mathcal{B}) < 3$) for the PLRN model. It also does

not take into account the information that can be gained by including the full posterior distribution for σ_{RN} during the fitting.

We can overcome these shortcomings by assuming our measurements of σ_{RN} for a given pulsar is drawn from a Gaussian distribution, the mean of which depends on the aforementioned scaling of the pulsars spin and spin-down frequencies (equation 25), and a variance ε^2 defined by

$$\pi(\sigma_{\text{RN}} | \chi_{\text{RN}}, \varepsilon) = \frac{1}{\sqrt{2\pi\varepsilon^2}} \exp \left[-\frac{(\sigma_{\text{RN}} - \chi_{\text{RN}})^2}{2\varepsilon^2} \right]. \quad (30)$$

This distribution represents an approximation to the ‘true’ probability distribution of σ_{RN} across the population. To compute the posterior distributions for our scaling hyper-parameters ($\{\xi, a, b, \gamma\}$), we use the marginalized likelihood

$$\mathcal{L}(\mathbf{r} | \chi_{\text{RN}}, \varepsilon) = \int d\sigma_{\text{RN}} \mathcal{L}(r | \sigma_{\text{RN}}) \pi(\sigma_{\text{RN}} | \chi_{\text{RN}}, \varepsilon). \quad (31)$$

As we are using an ensemble of N individual pulsars with residuals $\mathbf{r} = \{r_1, \dots, r_N\}$, we can take the product of the individual likelihoods to obtain the total likelihood of the timing data given the red noise strength for the population

$$\mathcal{L}_{\text{tot}}(\mathbf{r} | \sigma_{\text{RN}}) = \prod_i^N \mathcal{L}(r_i | \sigma_{\text{RN},i}), \quad (32)$$

hence the total marginalized likelihood can be rewritten as

$$\mathcal{L}_{\text{tot}}(\mathbf{r} | \chi_{\text{RN}}, \varepsilon) = \prod_i^N \int d\sigma_{\text{RN},i} \mathcal{L}(r_i | \sigma_{\text{RN},i}) \pi(\sigma_{\text{RN},i} | \chi_{\text{RN},i}, \varepsilon). \quad (33)$$

From Bayes theorem, we can find $\mathcal{L}(r_i | \sigma_{\text{RN},i})$ as

$$\mathcal{L}(r_i | \sigma_{\text{RN},i}) = \mathcal{Z}(r_i) \frac{p(\sigma_{\text{RN},i} | r_i)}{\pi(\sigma_{\text{RN},i})}, \quad (34)$$

Table 6. Comparison between recovered maximum likelihood posterior values for the scaling hyper-parameters and their associated 95 percent confidence intervals.

Parameter	mSC10 (RN+UL)	Hyper-PE (RN)	Hyper-PE (All)
$\log_{10}(\xi)$	$0.6^{+4.3}_{-4.4}$	$1.0^{+3.4}_{-3.0}$	$3.7^{+2.4}_{-2.7}$
a	$-0.87^{+0.83}_{-0.91}$	$-0.88^{+0.63}_{-0.60}$	$-0.84^{+0.47}_{-0.49}$
b	0.69 ± 0.29	$0.77^{+0.21}_{-0.22}$	$0.97^{+0.16}_{-0.19}$
γ	1.00 ± 2.17	$2.1^{+2.0}_{-1.8}$	1.0 ± 1.2
ε	$0.60^{+0.11}_{-0.16}$	$0.56^{+0.10}_{-0.12}$	$0.64^{+0.11}_{-0.16}$

where the prior on $\sigma_{\text{RN},i}$ is the product of the log-uniform prior on A and the uniform prior on β

$$\pi(\sigma_{\text{RN}}) = \pi(A, \beta) = \pi(A)\pi(\beta) = \frac{1}{A}, \quad (35)$$

for $A \in \{10^{-20}, 10^{-3}\}$. We then substitute equation 34 into equation 33 to obtain

$$\mathcal{L}(\mathbf{r}|\chi_{\text{RN}}, \varepsilon) = \int d\sigma_{\text{RN},i} \mathcal{Z}(r_i) p(\sigma_{\text{RN},i}|r_i) \frac{\pi(\sigma_{\text{RN},i}|\chi_{\text{RN},i}, \varepsilon)}{\pi(\sigma_{\text{RN},i})}. \quad (36)$$

Converting the integral over $\sigma_{\text{RN},i}$ to a sum over the posterior samples, as $\int dx p(x)f(x) \approx 1/n_s \sum_{i=1}^{n_s} f(x_i)$ (Hogg & Foreman-Mackey 2018), the final likelihood function is

$$\mathcal{L}(\mathbf{r}|\chi_{\text{RN}}, \varepsilon) = \prod_i \frac{\mathcal{Z}(r_i)}{n_i} \sum_k \frac{\pi(\sigma_{\text{RN},i,k}|\chi_{\text{RN},i}, \varepsilon)}{\pi(\sigma_{\text{RN},i,k})}, \quad (37)$$

where k is the number of posterior samples for the i -th pulsar. We can then combine this likelihood with the prior for the hyper-parameters, $\pi(\chi_{\text{RN}}, \varepsilon)$, and the Bayesian evidence for the timing data, to obtain the posterior distributions for the hyper-parameters

$$p(\chi_{\text{RN}}, \varepsilon|\mathbf{r}) = \frac{\mathcal{L}(\mathbf{r}|\chi_{\text{RN}}, \varepsilon)\pi(\chi_{\text{RN}}, \varepsilon)}{\mathcal{Z}(\mathbf{r})}. \quad (38)$$

As with equation 29, the posterior distributions are sampled using PYMULTINEST. We present the resulting one- and two-dimensional posterior distributions in Fig. 5, comparing results from the mSC10 method, hyper-parameter estimation (Hyper-PE) using only the 112 non-recycled pulsars that favour the PLRN model, and the resulting improvement when all 280 non-recycled pulsars are included in the Hyper-PE method regardless of the preferred model.

Recovered values for each scaling hyper-parameter from both methods are listed in Table 6. It is clear the Hyper-PE method returns improved estimates over the mSC10 method (with the exception of ε , which is consistent between all three methods), as indicated by the smaller confidence regions. Including the additional 168 white noise dominated pulsars provides additional improvements, as the Hyper-PE method takes into account additional information by summing over the entire posterior distribution of σ_{RN} , rather than only using the maximum likelihood posterior value. Our recovered value of ε differs from the value of $\varepsilon = 1.6 \pm 0.1$ reported by Shannon & Cordes (2010). This inconsistency could be due to the use of two different methods of modelling timing noise in pulsars, resulting in a different amount of measurement scatter.

We can compare our results to those in the literature by looking at the specific scaling relation from equation 20. From our Hyper-PE method, we find the timing noise strength of the non-recycled pulsars in our sample follow the scaling relation

$$\chi_{\text{RN}} \propto \nu^{-0.84^{+0.47}_{-0.49}} |\dot{\nu}|^{0.97^{+0.16}_{-0.19}}. \quad (39)$$

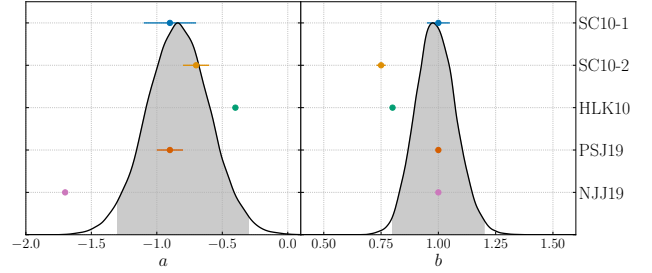


Figure 6. Comparison between our Hyper-PE (All) posteriors for a and b (black curves, shading represents the 95 percent confidence regions), and values (with $1\text{-}\sigma$ errors) from Shannon & Cordes (2010) (SC10-1: $\sigma_{\text{TN},2}$ and SC10-2: $\sigma_{\mathcal{A},2}$), Hobbs et al. (2010) (HLK10), Parthasarathy et al. (2019) (PSJ19) and Namkham et al. (2019) (NJJ19).

Shannon & Cordes (2010) computed a scaling relation of $\sigma_{\text{TN},2} \propto \nu^{-0.9 \pm 0.2} |\dot{\nu}|^{1.0 \pm 0.05}$, or $\sigma_{\mathcal{A},2} \propto \nu^{-0.7 \pm 0.1} |\dot{\nu}|^{0.76 \pm 0.02}$ when including the effects of additional white noise, while the analysis by Hobbs et al. (2010) found the relation $\sigma_z(10 \text{ yr}) = 10^{-11.5} \nu^{-0.4} |\dot{\nu}_{-15}|^{0.8}$, where $|\dot{\nu}_{-15}|$ is the spin-down rate in units of 10^{-15} s^{-2} . More recently, Parthasarathy et al. (2019) made use of TEMPO_{NEST}, and the same timing noise strength metric we used, to analyse 85 ‘young’ ($\tau_c \lesssim 1 \text{ Myr}$), high- \dot{E} pulsars with ~ 10 years of timing observations. Using a grid search to find the maximally correlated ν scaling index – at a fixed scaling parameter of 1 for $\dot{\nu}$ – they found a scaling relation of $\sigma_P \propto \nu^{-0.9 \pm 0.1} |\dot{\nu}|^1$. This same grid search method was also used by Namkham et al. (2019) to infer their scaling of the σ_z parameter, obtaining the relation $\sigma_P \propto \nu^{-1.7} |\dot{\nu}|^{1.0}$.

The values of a and b from each of these relations are compared with our results in Fig. 6. Our relation is entirely consistent with Shannon & Cordes (2010)’s $\sigma_{\text{TN},2}$ scaling, while both relations from Hobbs et al. (2010) and Parthasarathy et al. (2019) fall within our 95-percent confidence regions. Improving our measurements of a and b can be achieved by adding additional pulsars to our sample and/or by extending the lengths of our timing baselines. The improvement made by adding more pulsars is illustrated by the ~ 22 percent reduction in the Hyper-PE confidence regions in Fig. 5 after including the 168 pulsars that favour the WTN model in our analysis. Additional observations over longer timing baselines may allow us to obtain improved red noise amplitude and spectral index measurements, and detect low amplitude red noise in pulsars that currently favour the WTN model.

Applying a consistent approach to measuring timing noise strength in various data sets is of particular importance when it comes to comparing observations with theoretical models of timing noise processes. Our method of performing parameter estimation on the stochastic properties of individual pulsars with TEMPO_{NEST} followed by using hyper-parameter estimation to infer the scaling across the population can be easily extended to other large pulsar timing programmes, or even modified to accommodate astrophysically motivated distributions on the expected spectral properties of timing noise (see, e.g Melatos & Link 2014). Model selection studies could also allow for different physical timing noise models to be compared, along with their implications for our understanding of the dynamic processes and internal structure of neutron stars.

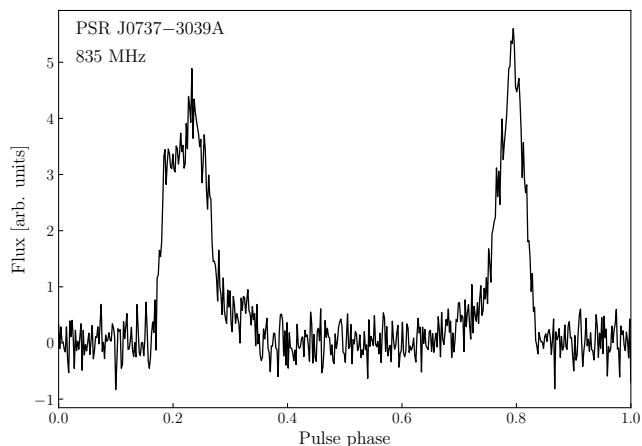


Figure 7. Average pulse profile of PSR J0737–3039A at 835 MHz after summing 71.1 hours worth of observations taken over four years.

5.4 Two noteworthy pulsars

Here we discuss results for two pulsars of particular interest: PSR J0737–3039A, for which we constrain the decay of its orbital period due to gravitational-wave emission, and PSR J1402–5124, whose celestial coordinates we find to be different to published values.

PSR J0737–3039A

J0737–3039A is the ‘A’ pulsar of the renowned double pulsar system discovered by Burgay et al. (2003). The ‘B’ pulsar (Lyne et al. 2004) is currently not visible due to its magnetic-axis precessing out of our line-of-sight (Perera et al. 2010). As its name suggests, the double pulsar allowed a determination of the mass ratio R by measuring the two semi-major axes of the pulsars. When combined with the sum of the masses derived from the advance of periastron, this completely determines the constituent masses to high precision, and predicts the rate of orbital decay due to the emission of gravitational waves. Using TEMPO_NEST to conduct parameter estimation on the pulsar’s rotational and binary parameters, we find the relativistic properties of the system to be consistent with the masses and GR parameters measured by Kramer et al. (2006b). This produces the integrated profile seen in Fig. 7. The (albeit limited) timing precision is good enough for us to spot any potential glitches in the pulsar’s rotation, assist in dispersion measure variation monitoring, and to be used in undergraduate projects to demonstrate post-Keplerian effects such as advance of periastron and orbital decay to better than 1 percent accuracy.

PSR J1402–5124

During our regular FRB-search transit observations, the real-time detection pipeline reported a candidate pulse from an unknown source with a DM of 53 pc cm^{-3} and a S/N of 10.2 at MJD 58657.40992245. Upon inspection of the data, we detected many faint single pulses with similar morphology drifting through our fan-beams. A periodicity search on the data ‘stitched’ according to the sky-drift-rate revealed a high S/N pulsar candidate with a period of 1.38 s and $\text{DM} = 51(9) \text{ pc cm}^{-3}$, closely matching the properties of pulsar PSR J1402–5124 reported by Manchester et al. (1978). A first-order localisation of the source, however, yielded a sky position that was inconsistent with the coordinates reported in the pulsar catalogue. Tracking the source using finely-spaced

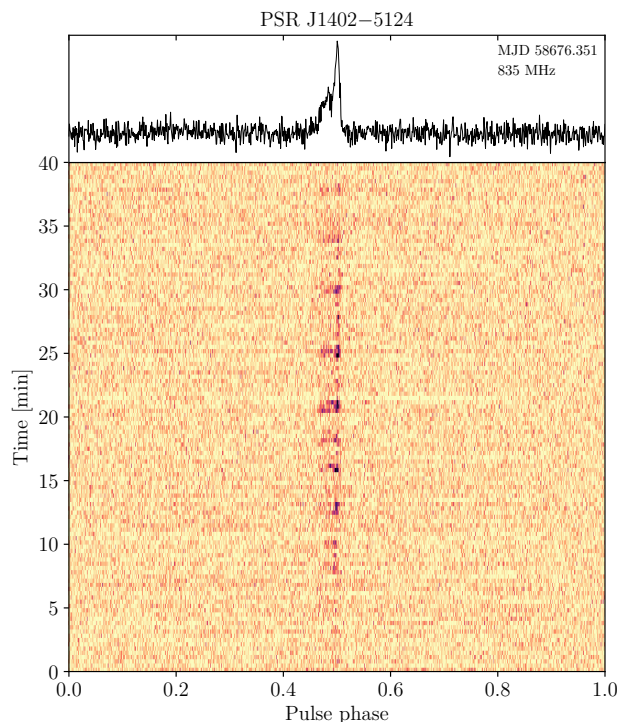


Figure 8. Stack of 20 s sub-integrations over 40 minutes (bottom) and the integrated pulse profile (top) of PSR J1402–5124 at 835 MHz. Brightening (dimming) of the pulsar toward the lower (upper) edge of the figure is due to the telescope’s beam response. Dynamic range has been reduced to highlight profile changes between sub-integrations.

fan-beams over the next few days, we optimized the coordinates of the pulsar to: RA = 14:02:56.0(2), DEC = $-50:21:43(49)$. The improved declination measurement is consistent with the value of DEC = $-50:20(5)$ reported by Edwards et al. (2001). In Fig. 8 we highlight the variability of the pulse profile by plotting the phase vs time of the pulsar throughout a 40 minute observation after placing a tied-array-beam on the updated coordinates. Using 5 epochs of timing observations, we are able to constrain the spin-period of the pulsar to $P = 1.380182295(4) \text{ s}$. Subtracting this new period measurement from the value reported in Manchester et al. (1978) we derive an estimated spin-down of $\dot{P} = -5.413(4) \times 10^{-15}$, placing it in the population of ‘middle-aged’ pulsars ($\tau_c \approx 4 \text{ Myr}$). The astrometric and rotational properties will be further constrained as we continue to time the pulsar.

6 CONCLUSIONS

We have performed an initial study of the rotational properties of 300 bright, southern-sky radio pulsars observed by UTMOST using the Bayesian pulsar timing software TEMPO_NEST to characterise the stochastic properties of our pulsar sample and to obtain unbiased measurements of ν and $\dot{\nu}$. Three millisecond pulsars in our sample favour the Power-Law Red Noise (PLRN) model, but this excess noise is due to a combination of instrumental artefacts and extrinsic astrophysical sources as opposed to rotational irregularities.

We also used TEMPO_NEST to reanalyse nine previously reported pulsar glitches. While the posterior distributions we recover for the change in spin-frequency are generally consistent with previously published values, we are able to place tighter constraints on the

change in spin-down and spin-recovery. Performing model selection, we find a PLRN-only model is preferred for two previously reported glitches, one in PSR J0835–4510 on MJD 56922(3) and PSR J1740–3015 on MJD 57346.0(6). This highlights the importance of accounting for timing noise of a pulsar when estimating glitch properties, and the potential use of model selection as a means of verifying glitch detections any additional, undiscovered glitch/micro-glitch candidates that may be present in the data. It also indicates conducting reliable parameter estimation on micro-glitch candidates in the presence of strong red noise is difficult. We also present the discovery of a new glitch in PSR J1452–6036 and the first ever glitch observed in PSR J1703–4851. Additionally, we observed four unusual glitch-like events in PSR J1825–0935, the larger of which cannot be adequately explained by timing noise alone. While it is possible the two large events were due to ‘slow glitches’, we have insufficient observations around their epochs to obtain high resolution measurements of $\dot{\nu}$. As a result, we do not observe a sharp increase in the spin-down typically associated with slow glitches.

Limiting ourselves to only the non-recycled pulsars in our sample, we find the strongest correlation between various pulsar properties and the relative red noise strength exists with pulsar spin-down (\dot{P}) and $\dot{\nu}$, with a similar anti-correlation with characteristic age. These correlations agree with recent work by Namkham et al. (2019), but are generally weaker than those found by Hobbs et al. (2010). We conclude this difference is likely caused by Hobbs et al. (2010) including millisecond pulsars in their analysis, while we are limited to non-recycled pulsars. Building on work by Shannon & Cordes (2010), we developed a new Bayesian hyper-parameter estimation (Hyper-PE) framework for inferring the scaling between red noise strength and pulsar spin-frequency and spin-down across the population. This relation can be used to estimate the expected red noise strength of a pulsar based on its measured spin and spin-down. Our inferred scaling relation of $\chi_{\text{RN}} \propto \nu^a |\dot{\nu}|^b$, where $a = -0.84_{-0.49}^{+0.47}$ and $b = 0.97_{-0.19}^{+0.16}$, is consistent with those found in previous studies by Shannon & Cordes (2010), Hobbs et al. (2010) and Parthasarathy et al. (2019). As timing noise strength scales with the length of each pulsar data span, applying our Hyper-PE method to a much larger data set with longer timing baselines will enable more stringent constraints to be placed on the scaling between timing noise strength and pulsar rotational properties. These data could be obtained by UTMOST in the future, or other large, long-term timing programmes such as those undertaken at Jodrell Bank and CHIME/Pulsar (Ng 2018). A natural extension of our study would be to include measurements of red noise in a large sample of millisecond pulsars and magnetars. In addition, the ability to perform model selection studies using astrophysically motivated noise models could allow us to place constraints on the precise mechanism behind spin noise.

Finally, we discussed the capability of UTMOST to contribute to the monitoring of relativistic binary systems such as the double pulsar PSR J0737–3039. We also used the interferometer nature of the instrument to measure an updated position for the bright, mode-changing pulsar PSR J1402–5124 in addition to providing the first estimate of this pulsar’s spin-down rate.

ACKNOWLEDGEMENTS

The Molonglo Observatory is owned and operated by the University of Sydney. Major support for the UTMOST project has been provided by Swinburne University of Technology. We acknowledge

the Australian Research Council grants CE110001020 (CAASTRO) and the Laureate Fellowship FL150100148. MEL acknowledges support from the Australian Government Research Training Program and CSIRO Astronomy and Space Science. FJ acknowledges funding from the European Research Council (ERC) under the European Union’s Horizon 2020 research and innovation programme (grant agreement No. 694745). This work made use of the gSTAR and OzSTAR national HPC facilities. gSTAR is funded by Swinburne and the Australian Government’s Education Investment Fund. OzSTAR is funded by Swinburne and the National Collaborative Research Infrastructure Strategy (NCRIS). We made use of the standard scientific Python packages (Oliphant 2006; Jones et al. 2001; McKinney 2010), MATPLOTLIB (Hunter 2007), PSRQPY (Pitkin 2018), BILBY (Ashton et al. 2019b), CHAINCONSUMER (Hinton 2016) and ASTROPY (Robitaille et al. 2013; Price-Whelan et al. 2018). We also acknowledge use of the Astronomer’s Telegram (ATel), NASA Astrophysics Data Service (ADS) and NASA/IPAC Extragalactic Database (NED). We give thanks to the anonymous referee for their helpful comments and suggestions.

REFERENCES

- Alpar M. A., Nandkumar R., Pines D., 1985, *ApJ*, **288**, 191
 Anderson P. W., Itoh N., 1975, *Nature*, **256**, 25
 Arzoumanian Z., Nice D. J., Taylor J. H., Thorsett S. E., 1994, *ApJ*, **422**, 671
 Ashton G., Lasky P. D., Graber V., Palfreyman J., 2019a, *Nature Astronomy*, p. 417
 Ashton G., et al., 2019b, *ApJS*, **241**, 27
 Bailes M., et al., 2017, *Publ. Astron. Soc. Australia*, **34**, e045
 Baym G., Pethick C., Pines D., Ruderman M., 1969, *Nature*, **224**, 872
 Blandford R. D., Romani R. W., 1988, *MNRAS*, **234**, 57P
 Bonazzola S.,ourgoulhon E., 1996, *A&A*, **312**, 675
 Brook P. R., Karastergiou A., Buchner S., Roberts S. J., Keith M. J., Johnston S., Shannon R. M., 2014, *ApJ*, **780**, L31
 Brook P. R., Karastergiou A., Johnston S., Kerr M., Shannon R. M., Roberts S. J., 2016, *MNRAS*, **456**, 1374
 Buchner S., 2013, *Astron. Telegram*, **5406**
 Buchner J., et al., 2014, *A&A*, **564**, A125
 Burgay M., et al., 2003, *Nature*, **426**, 531
 Caleb M., et al., 2017, *MNRAS*, **468**, 3746
 Camilo F., et al., 2018, *ApJ*, **856**, 180
 Cheng K. S., 1987a, *ApJ*, **321**, 799
 Cheng K. S., 1987b, *ApJ*, **321**, 805
 Chukwude A. E., 2007, *Chinese J. Astron. Astrophys.*, **7**, 521
 Chukwude A. E., Buchner S., 2012, *ApJ*, **745**, 40
 Coles W., Hobbs G., Champion D. J., Manchester R. N., Verbiest J. P. W., 2011, *MNRAS*, **418**, 561
 Cordes J. M., Downs G. S., 1985, *ApJS*, **59**, 343
 Cordes J. M., Helfand D. J., 1980, *ApJ*, **239**, 640
 Cordes J. M., Shannon R. M., 2008, *ApJ*, **682**, 1152
 Detweiler S., 1979, *ApJ*, **234**, 1100
 Dewey R. J., Cordes J. M., 1989, in Ögelman H., van den Heuvel E. P. J., eds, Vol. 262, NATO Advanced Sci. Institutes (ASI) Series C. p. 119
 Edwards R. T., Bailes M., van Straten W., Britton M. C., 2001, *MNRAS*, **326**, 358
 Edwards R. T., Hobbs G. B., Manchester R. N., 2006, *MNRAS*, **372**, 1549
 Espinoza C. M., Lyne A. G., Stappers B. W., Kramer M., 2011, *MNRAS*, **414**, 1679
 Farah W., et al., 2018, *MNRAS*, **478**, 1209
 Farah W., et al., 2019, *MNRAS*, p. 1717
 Feroz F., Hobson M. P., 2008, *MNRAS*, **384**, 449
 Feroz F., Hobson M. P., Bridges M., 2009, *MNRAS*, **398**, 1601
 Folkner W. M., Williams J. G., Boggs D. H., Park R. S., Kuchynka P., 2014, *Interplanetary Network Progress Report*, **42-196**, 1

- Fowler L. A., Wright G. A. E., Morris D., 1981, *A&A*, **93**, 54
- Gil J. A., et al., 1994, *A&A*, **282**, 45
- Greenstein G., 1970, *Nature*, **227**, 791
- Gunn J. E., Ostriker J. P., 1969, *Nature*, **221**, 454
- Gupta V., et al., 2019a, *Astron. Telegram*, **12610**
- Gupta V., et al., 2019b, *Astron. Telegram*, **12995**
- Gupta V., et al., 2019c, *Astron. Telegram*, **13282**
- Gupta V., et al., 2019d, *Astron. Telegram*, **13363**
- Harding A. K., Contopoulos I., Kazanas D., 1999, *ApJ*, **525**, L125
- Hellings R. W., Downs G. S., 1983, *ApJ*, **265**, L39
- Hinton S. R., 2016, *The Journal of Open Source Software*, **1**, 00045
- Hobbs G., Lorimer D. R., Lyne A. G., Kramer M., 2005, *MNRAS*, **360**, 974
- Hobbs G. B., Edwards R. T., Manchester R. N., 2006, *MNRAS*, **369**, 655
- Hobbs G., Lyne A. G., Kramer M., 2010, *MNRAS*, **402**, 1027
- Hogg D. W., Foreman-Mackey D., 2018, *ApJS*, **236**, 11
- Hotan A. W., van Straten W., Manchester R. N., 2004, *Publ. Astron. Soc. Australia*, **21**, 302
- Hunter J. D., 2007, *Comput. in Sci. & Eng.*, **9**, 90
- Jankowski F., et al., 2015a, *Astron. Telegram*, **6903**
- Jankowski F., et al., 2015b, *Astron. Telegram*, **8298**
- Jankowski F., et al., 2016, *Astron. Telegram*, **9054**
- Jankowski F., et al., 2017, *Astron. Telegram*, **10770**
- Jankowski F., et al., 2019, *MNRAS*, **484**, 3691
- Jetten F. A., Anderson S. B., Kaspi V. M., Prince T. A., Unwin S. C., 1998, *The Astrophysical Journal*, **498**, 365
- Jetten F. A., et al., 2006, *ApJ*, **653**, 1571
- Johnston S., Galloway D., 1999, *MNRAS*, **306**, L50
- Jones P. B., 1990, *MNRAS*, **246**, 364
- Jones E., et al., 2001, SciPy: Open source scientific tools for Python, <http://www.scipy.org/>
- Kass R. E., Raftery A. E., 1995, *J. of the American Statistical Association*, **90**, 773
- Keith M. J., et al., 2013, *MNRAS*, **429**, 2161
- Kerr M., 2019, *The Astronomer's Telegram*, **12481**
- Kerr M., Johnston S., Hobbs G., Shannon R. M., 2015, *ApJ*, **809**, L11
- Kerr M., Hobbs G., Johnston S., Shannon R. M., 2016, *MNRAS*, **455**, 1845
- Kramer M., Lyne A. G., O'Brien J. T., Jordan C. A., Lorimer D. R., 2006a, *Science*, **312**, 549
- Kramer M., et al., 2006b, *Science*, **314**, 97
- Lentati L., Shannon R. M., 2015, *MNRAS*, **454**, 1058
- Lentati L., Alexander P., Hobson M. P., Taylor S., Gair J., Balan S. T., van Haasteren R., 2013, *Phys. Rev. D*, **87**, 104021
- Lentati L., Alexander P., Hobson M. P., Feroz F., van Haasteren R., Lee K. J., Shannon R. M., 2014, *MNRAS*, **437**, 3004
- Lentati L., et al., 2016, *MNRAS*, **458**, 2161
- Link B., 2012, *MNRAS*, **422**, 1640
- Liu J., Yan Z., Yuan J.-P., Zhao R.-S., Huang Z.-P., Wu X.-J., Wang N., Shen Z.-Q., 2019, *Research in Astronomy and Astrophysics*, **19**, 073
- Lower M. E., et al., 2018, *Res. Notes of the AAS*, **2**, 139
- Lower M. E., et al., 2019, *Res. Notes of the AAS*, **3**, 192
- Lyne A. G., et al., 2004, *Science*, **303**, 1153
- Lyne A., Hobbs G., Kramer M., Stairs I., Stappers B., 2010, *Science*, **329**, 408
- Lyne A., Graham-Smith F., Weltevrede P., Jordan C., Stappers B., Bassa C., Kramer M., 2013, *Science*, **342**, 598
- Manchester R. N., Lyne A. G., Taylor J. H., Durdin J. M., Large M. I., Little A. G., 1978, *MNRAS*, **185**, 409
- Manchester R. N., Hobbs G. B., Teoh A., Hobbs M., 2005, *AJ*, **129**, 1993
- Manchester R. N., et al., 2013, *Publ. Astron. Soc. Australia*, **30**, e017
- Matsakis D. N., Taylor J. H., Eubanks T. M., 1997, *A&A*, **326**, 924
- McKinney W., 2010, *Proc. of the 9th Python in Sci. Conf.*, 51-56
- Melatos A., Link B., 2014, *MNRAS*, **437**, 21
- Melatos A., Peralta C., Wyithe J. S. B., 2008, *ApJ*, **672**, 1103
- Morello V., et al., 2018, *MNRAS*,
- Morris D., Graham D. A., Bartel N., 1981, *MNRAS*, **194**, 7P
- Namkham N., Jaroenjittichai P., Johnston S., 2019, *MNRAS*, **p. 1636**
- Ng C., 2018, in *Pulsar Astrophysics the Next Fifty Years*. pp 179–182, [doi:10.1017/S1743921317010638](https://doi.org/10.1017/S1743921317010638)
- Oliphant T., 2006, *NumPy: A guide to NumPy, USA: Trelgol Publishing*, <http://www.numpy.org/>
- Palfreyman J. L., Dickey J. M., Ellingsen S. P., Jones I. R., Hotan A. W., 2016, *ApJ*, **820**, 64
- Palfreyman J., Dickey J. M., Hotan A., Ellingsen S., van Straten W., 2018, *Nature*, **556**, 219
- Parthasarathy A., et al., 2019, *MNRAS*, **489**, 3810
- Perera B. B. P., et al., 2010, *ApJ*, **721**, 1193
- Petroff E., Keith M. J., Johnston S., van Straten W., Shannon R. M., 2013, *MNRAS*, **435**, 1610
- Pitkin M., 2018, *J. Open Source Software*, **3**, 538
- Price-Whelan A. M., et al., 2018, *Astron. J.*, **156**, 123
- Reardon D. J., Coles W. A., Hobbs G., Ord S., Kerr M., Bailes M., Bhat N. D. R., Venkatraman Krishnan V., 2019, *MNRAS*, **485**, 4389
- Robitaille T. P., et al., 2013, *Astron. Astrophys.*, **558**, A33
- Ruderman M., 1969, *Nature*, **223**, 597
- Sarkissian J. M., Reynolds J. E., Hobbs G., Harvey-Smith L., 2017, *Publ. Astron. Soc. Australia*, **34**, e027
- Sarkissian J., Hobbs G., Reynolds J., Palfreyman J., Olney S., 2019, *The Astronomer's Telegram*, **12466**, 1
- Shabanova T. V., 2007, *Ap&SS*, **308**, 591
- Shannon R. M., Cordes J. M., 2010, *ApJ*, **725**, 1607
- Shannon R. M., Lentati L. T., Kerr M., Johnston S., Hobbs G., Manchester R. N., 2016, *MNRAS*, **459**, 3104
- Shapiro S. L., Teukolsky S. A., 1983, *Black holes, white dwarfs, and neutron stars : the physics of compact objects*. Wiley-VCH
- Skilling J., 2004, *AIP Conf. Proc.*, **735**, 395
- Staelin D. H., Reifenshtein Edward C. I., 1968, *Science*, **162**, 1481
- Stairs I. H., Lyne A. G., Shemar S. L., 2000, *Nature*, **406**, 484
- Taylor J. H., 1992, *Philosophical Transactions of the Royal Society of London Series A*, **341**, 117
- Thrane E., Talbot C., 2019, *Publ. Astron. Soc. Australia*, **36**, e010
- Urama J. O., Link B., Weisberg J. M., 2006, *MNRAS*, **370**, L76
- Venkatraman Krishnan V., et al., 2020, *MNRAS*, **p. 108**
- Wang N., Manchester R. N., Johnston S., 2007, *MNRAS*, **377**, 1383
- Yu M., et al., 2013, *MNRAS*, **429**, 688
- Yue Y. L., Xu R. X., Zhu W. W., 2007, *Advances in Space Res.*, **40**, 1491
- Zou W. Z., Wang N., Wang H. X., Manchester R. N., Wu X. J., Zhang J., 2004, *MNRAS*, **354**, 811
- van Haasteren R., Levin Y., 2013, *MNRAS*, **428**, 1147
- van Straten W., Bailes M., 2011, *Publ. Astron. Soc. Australia*, **28**, 1
- van Straten W., Demorest P., Osłowski S., 2012, *Astronomical Research and Technology*, **9**, 237

APPENDIX A: PULSAR ASTROMETRIC AND SPIN PARAMETERS

We list the measured astrometric and rotational parameters for each pulsar in our sample in Table A1.

Table A1. Astrometric and rotational parameters of all pulsars analysed in this work, including the sky-locations in equatorial coordinates, spin frequencies, spin-down and second spin-frequency derivative. The period, position and DM epoch is MJD 57600 for all pulsars. Errors for RAJ and DEC represent the one-sigma uncertainty on the last digit from TEMPO2. Uncertainties on ν and $\dot{\nu}$ represent the 95 percent confidence intervals scaled to the last digit. Flags indicate: PPTA – pulsar is observed as part of the Parkes Pulsar Timing Array project (Manchester et al. 2013), B – pulsar is in a binary. The full table contains 300 pulsars and is available in the supplementary material.

PSRJ	RAJ (hh:mm:ss)	DECJ (°:′:″)	ν (Hz)	$\dot{\nu}$ (10^{-15} s^{-2})	$\ddot{\nu}$ (10^{-24} s^{-3})	N_{ToA}	T (yr)	Flags
J0030+0451	00:30:27.423(9)	+04:51:39.7(3)	205.530699027(+7, −8)	−0.39(±1)	–	58	1.04	–
J0134−2937	01:34:18.6939(2)	−29:37:17.157(5)	7.30131486798(±8)	−4.17767(±2)	(±0.1)	198	3.42	–
J0151−0635	01:51:22.718(4)	−06:35:02.98(1)	0.682750032508(+6, −5)	−0.20585(±2)	(+0.038, −0.2)	196	3.74	–
J0152−1637	01:52:10.854(1)	−16:37:53.63(3)	1.20085114658(+7, −9)	−1.87464(+2, −3)	(+0.064, −0.098)	119	3.29	–
J0206−4028	02:06:01.2931(1)	−40:28:03.616(1)	1.58591388856(±5)	−3.01013(±2)	(+0.1, −0.08)	131	3.35	–
J0255−5304	02:55:56.2939(4)	−53:04:21.250(4)	2.23359632409(±2)	−0.155852(+7, −8)	(+0.038, −0.054)	270	3.75	–
J0348+0432	03:48:43.639(3)	+04:32:11.45(2)	25.5606365903(+4, −5)	−0.158(±2)	(+26.2, −14.7)	41	2.85	B
J0401−7608	04:01:51.75(1)	−76:08:12.95(5)	1.83400700914(+9, −7)	−5.1927(+3, −4)	(+0.9, −0.4)	110	3.15	–
J0418−4154	04:18:03.7748(4)	−41:54:14.42(6)	1.32079643042(±2)	−2.30176(±6)	(+0.13, −0.58)	99	3.38	–
J0437−4715	04:37:15.8961(6)	−47:15:09.1107(3)	173.68794581(+2, −1)	−1.72(+3, −4)	–	230	1.41	PPTA, B
J0450−1248	04:50:08.7903(2)	−12:48:07.088(8)	2.28303085312(+6, −4)	−0.5358(±1)	(+1.7, −0.9)	81	3.14	–
J0452−1759	04:52:34.119(1)	−17:59:23.15(3)	1.82168155657(+5, −4)	−19.0941(+1, −3)	(+0.08, −0.45)	121	3.73	–
J0525+1115	05:25:56.498(1)	+11:15:18.8(1)	2.82137062404(±2)	−0.58697(+8, −7)	(+0.21, −0.58)	59	3.15	–
J0529−6652	05:29:50.90(3)	−66:52:39.9(3)	1.02486651379(+2, −1)	−16.2526(+3, −4)	(+20.7, −2.7)	59	2.24	–
J0533+0402	05:33:25.828(5)	+04:01:59.7(2)	1.03840237842(±2)	−0.17255(+8, −1)	(+0.46, −0.16)	54	3.14	–
J0536−7543	05:36:30.829(4)	−75:43:54.63(2)	0.802660896061(+1, −2)	−0.37076(±5)	(+0.06, −0.066)	189	3.63	–
J0601−0527	06:01:58.9731(8)	−05:27:50.92(2)	2.52544324442(+6, −7)	−8.30641(+3, −2)	(+0.085, −0.053)	208	3.72	–
J0624−0424	06:24:20.025(1)	−04:24:50.56(4)	0.962392542206(±1)	−0.769(±2)	(+0.12, −0.12)	120	3.14	–
J0627+0706	06:27:44.172(4)	+07:06:33.0(2)	2.10134828979(±1)	−131.6248(±5)	(+0.3, −1.5)	111	3.15	–
J0630−2834	06:30:49.35(1)	−28:34:42.1(2)	0.803583722117(+3, −2)	−4.6323(+1, −9)	(+0.16, −0.13)	87	3.65	–
J0646+0905	06:46:31.025(5)	+09:05:49.6(3)	1.10630072318(+7, −9)	−0.9009(±2)	(+1.3, −1.1)	160	3.01	–
J0659+1414	06:59:48.188(5)	+14:14:19.2(4)	2.59788422925(±2)	−370.7966(±9)	$1_{-0.5}^{+1.1}$	162	3.15	–
J0711−6830	07:11:54.1654(1)	−68:30:47.296(1)	182.117234537(+9, −1)	−0.4928(±3)	(+4.0, −2.5)	43	2.89	PPTA
J0729−1836	07:29:32.30(1)	−18:36:42.1(2)	1.96011842607(+2, −1)	−72.8289(+6, −7)	$-2_{-1.8}^{+2.4}$	169	3.16	–
J0737−3039A	07:37:51.24669(2)	−30:39:40.6895(3)	44.0540680812(+7, −6)	−3.4149(±3)	(+0.82, −0.63)	144	3.49	B
J0738−4042	07:38:32.244(3)	−40:42:39.43(4)	2.66723044109(±5)	−9.805(±2)	-3.5 ± 1.2	243	3.66	–
J0742−2822	07:42:48.91(4)	−28:22:44.0(7)	5.996127853(±2)	−604.187(±1)	(+1.0, −35.8)	180	3.46	–
J0758−1528	07:58:29.061(2)	−15:28:08.333(4)	1.46570344504(+3, −4)	−3.4786(+2, −1)	(+0.21, −0.28)	144	3.12	–

Table A1 – continued

PSRJ	RAJ (hh:mm:ss)	DECJ (°:′:″)	ν (Hz)	$\dot{\nu}$ (10^{-15} s^{-2})	$\ddot{\nu}$ (10^{-24} s^{-3})	N_{ToA}	T (yr)	Flags
J0809–4753	08:09:43.834(3)	–47:53:54.85(2)	1.82747830432(+6, –4)	–10.2748(±2)	(+0.07, –0.32)	79	3.12	–
J0820–1350	08:20:26.407(1)	–13:50:56.32(4)	0.807668884066(±4)	–1.37174(±2)	(+0.084, –0.09)	51	3.57	–
J0820–4114	08:20:15.46(1)	–41:14:35.2(1)	1.8333635346(±7)	–0.0664(±2)	(+0.48, –0.78)	88	3.39	–
J0835–4510	08:35:20.6(2)	–45:10:33(1)	11.18677868(±2)	–13161(+5.4, –5.3)	(+19949.0, –7024.5)	1420	4.81	–
J0837+0610	08:37:05.6462(1)	+06:10:15.87(6)	0.785068914181(+2, –3)	–4.19046(+1, –8)	(+0.033, –0.016)	78	3.75	–
J0837–4135	08:37:21.1922(4)	–41:35:14.589(4)	1.33044994223(±5)	–6.26572(±3)	(+0.038, –0.09)	140	3.64	–
J0840–5332	08:40:33.726(9)	–53:32:35.95(6)	1.38770592261(±3)	–3.154(±1)	(+0.09, –0.23)	59	3.14	–
J0842–4851	08:42:05.4443(9)	–48:51:20.6(1)	1.5519428595(±9)	–23.0246(+7, –8)	(+2.7, –0.1)	53	3.13	–
J0846–3533	08:46:06.0712(4)	–35:33:40.91(6)	0.895978340332(±1)	–1.28499(±4)	(+0.13, –0.3)	65	3.3	–
J0855–3331	08:55:38.421(3)	–33:31:38.99(4)	0.788929778283(+1, –2)	–3.93327(+4, –3)	(+0.2, –0.28)	76	3.12	–
J0856–6137	08:56:59.27(1)	–61:37:52.71(8)	1.03894958562(+2, –3)	–1.813(+1, –8)	(+0.33, –0.11)	48	3.39	–
J0904–4246	09:04:59.083(9)	–42:46:13.4(1)	1.03608336991(+3, –2)	–2.0148(+9, –1)	(+0.24, –0.4)	50	3.37	–
J0904–7459	09:04:10.47(3)	–74:59:41.7(1)	1.81965845843(+1, –7)	–1.5278(+4, –3)	(+1.1, –1.0)	44	2.98	–
J0907–5157	09:07:15.901(3)	–51:57:59.36(2)	3.9438751026(+7, –5)	–28.5412(±3)	(+0.87, –0.12)	121	3.5	–
J0908–1739	09:08:38.227(4)	–17:39:39.9(1)	2.48987780015(±4)	–4.1492(±2)	(+0.27, –0.98)	37	3.16	–
J0908–4913	09:08:35.46(1)	–49:13:05.00(1)	9.36601123448(±6)	–1324.821(+3, –4)	$4_{-1.5}^{+1.3}$	173	3.48	–
J0909–7212	09:09:35.81(3)	–72:12:08.94(1)	0.733734742115(±4)	–0.1762(±2)	(+0.15, –0.41)	31	3.15	–
J0922+0638	09:22:13.85(3)	+06:38:19(1)	2.32217901642(±3)	–73.985(±1)	(+2.5, –9.6)	68	3.02	–
J0924–5302	09:24:08.722(4)	–53:02:42.6(3)	1.33987540461(±2)	–63.431(+1, –9)	(+3.9, –4.1)	137	3.2	–
J0924–5814	09:24:30.82(1)	–58:14:05.10(1)	1.35225504146(+4, –3)	–9.0013(±2)	(+0.48, –0.28)	72	3.39	–
J0934–5249	09:34:28.237(5)	–52:49:27.30(5)	0.692148271001(+1, –8)	–2.22898(±3)	(+0.07, –0.14)	152	3.16	–
J0942–5552	09:42:14.88(6)	–55:52:55.1(5)	1.50514304056(±3)	–51.376(±2)	$8_{-4.3}^{+4.1}$	150	3.69	–
J0942–5657	09:42:54.422(5)	–56:57:43.21(3)	1.23737204376(±4)	–60.6357(±2)	(+0.37, –0.09)	90	3.18	–
J0944–1354	09:44:28.967(1)	–13:54:41.88(2)	1.75357327379(+5, –7)	–0.13929(±2)	(+0.069, –0.118)	61	3.11	–
J0953+0755	09:53:09.3121(2)	+07:55:36.9(1)	3.95154788907(+9, –8)	–3.58768(±3)	(+0.021, –0.07)	73	3.71	–
J0955–5304	09:55:29.461(1)	–53:04:16.64(1)	1.15992862694(±4)	–4.74318(±1)	(+0.16, –0.078)	155	3.26	–
J0959–4809	09:59:26.212(6)	–48:09:47.47(7)	1.49234604(+5, –4)	–0.1887(+1, –9)	(+0.49, –0.27)	78	3.37	–
J1001–5507	10:01:37.85(5)	–55:07:07.8(5)	0.696073036122(+9, –1)	–24.9925(+7, –6)	$1_{-1.6}^{+0.8}$	138	3.7	–
J1003–4747	10:03:21.529(1)	–47:47:01.190(2)	3.25654170022(±3)	–21.96544(+9, –6)	(+0.29, –0.36)	69	3.13	–
J1012–5857	10:12:48.470(5)	–58:57:48.50(3)	1.21962189426(±1)	–26.47184(±4)	(+0.05, –0.23)	193	3.71	–

Table A1 – continued

PSRJ	RAJ (hh:mm:ss)	DECJ (°:′:″)	ν (Hz)	$\dot{\nu}$ (10^{-15} s^{-2})	$\ddot{\nu}$ (10^{-24} s^{-3})	N_{ToA}	T (yr)	Flags
J1013–5934	10:13:31.848(2)	–59:34:26.63(1)	2.25784124141(± 1)	–2.83682(+3, –4)	(+0.12, –0.18)	132	3.43	–
J1016–5345	10:16:31.135(4)	–53:45:14.26(3)	1.29940016176(± 2)	–3.25316(+6, –4)	(+0.24, –0.8)	102	3.14	–
J1017–5621	10:17:12.831(1)	–56:21:30.517(7)	1.98624477638(± 5)	–12.38704(± 2)	(+0.2, –0.052)	127	3.17	B
J1017–7156	10:17:51.3172(5)	–71:56:41.596(2)	427.621905026(± 2)	–0.415(+1, –8)	(+10.3, –5.6)	51	3.38	B
J1022+1001	10:22:58.3(1)	+10:01:58(5)	60.7794479207(+6, –9)	–0.1564(± 3)	(+0.36, –0.52)	39	3.43	PPTA
J1032–5911	10:32:04.876(1)	–59:11:54.8(1)	2.15418526489(+2, –3)	–8.3414(± 5)	(+4.9, –0.4)	152	2.51	–
J1034–3224	10:34:19.46(1)	–32:24:26.2(2)	0.869118880561(+3, –2)	–0.17372(± 1)	(+0.14, –0.14)	41	3.74	–
J1036–4926	10:36:13.121(7)	–49:26:21.2(1)	1.95936510762(± 1)	–6.3385(± 3)	(+6.1, –7.5)	30	2.36	–
J1041–1942	10:41:36.191(9)	–19:42:13.7(2)	0.721308789858(+2, –3)	–0.4925(± 1)	(+0.12, –0.13)	34	3.41	–
J1042–5521	10:42:00.4853(9)	–55:21:05.793(6)	0.854067790376(± 2)	–4.89999(+6, –5)	(+0.24, –0.14)	101	3.36	–
J1043–6116	10:43:55.222(8)	–61:16:51.29(8)	3.46491578971(+8, –7)	–124.947(± 2)	(+77.6, –108.0)	78	1.47	–
J1045–4509	10:45:50.1794(5)	–45:09:54.106(6)	133.79314947(± 2)	–0.3153(+8, –6)	(+2.0, –1.0)	38	3.31	PPTA, B
J1046–5813	10:46:18.815(2)	–58:13:51.89(2)	2.70688676045(± 1)	–8.4(+4, –3)	(+0.48, –0.5)	193	3.25	–
J1047–6709	10:47:28.285(5)	–67:09:51.61(4)	5.0389844311(± 1)	–42.8418(+4, –3)	(+0.9, –1.2)	39	2.43	–
J1048–5832	10:48:13.1(1)	–58:32:03(1)	8.0824185121(+4, –5)	–6273.49(+2, –3)	$90^{+41.8}_{-51.2}$	232	3.44	–
J1056–6258	10:56:25.53(1)	–62:58:47.7(1)	2.36714106203(± 1)	–20.057(+8, –7)	(+0.9, –1.0)	198	3.69	–
J1057–5226	10:57:59.068(8)	–52:26:56.10(8)	5.0731886204(+2, –3)	–150.205(+2, –1)	(+0.1, –5.6)	126	2.62	–
J1057–7914	10:57:27.7(1)	–79:14:23.6(3)	0.74216802567(+8, –7)	–0.7321(+4, –3)	(+1.4, –0.8)	41	2.84	–
J1059–5742	10:59:00.8886(4)	–57:42:14.55(3)	0.843879990895(+1, –8)	–3.0668(± 3)	(+0.08, –0.31)	178	3.18	–
J1105–6107	11:05:26.2(1)	–61:07:48.0(8)	15.8222513283(+4, –3)	–3966.97(± 1)	(+6.0, –31.4)	145	2.85	–
J1110–5637	11:10:00.3712(6)	–56:37:32.57(4)	1.79129810299(+1, –2)	–6.6125(+8, –4)	(+1.8, –0.2)	130	3.17	–
J1112–6613	11:12:38.414(4)	–66:13:04.663(2)	2.9920963178(+5, –3)	–7.385(+1, –2)	(+0.1, –1.6)	96	2.93	–
J1112–6926	11:12:50.78(1)	–69:26:32.33(6)	1.21878739947(+4, –3)	–4.1912(± 1)	(+0.52, –0.6)	97	3.22	–
J1114–6100	11:14:22.69(5)	–61:00:32.1(3)	1.13525643826(± 2)	–59.3019(+6, –5)	(+4.8, –4.2)	137	2.45	–
J1116–4122	11:16:43.083(4)	–41:22:44.86(8)	1.06026074416(+2, –3)	–8.955(± 1)	(+0.04, –0.27)	47	3.53	–
J1121–5444	11:21:19.23(1)	–54:44:04.90(1)	1.86641502454(± 2)	–9.7309(+7, –8)	(+2.2, –3.8)	117	2.98	–
J1123–6259	11:23:55.53(1)	–62:59:10.92(8)	3.68409189328(± 1)	–71.2863(+3, –4)	(+5.3, –6.1)	70	2.99	–
J1126–6942	11:26:21.66(4)	–69:42:15.8(1)	1.72586751278(+3, –2)	–9.8111(+9, –1)	-0.69^{+6}_{-2}	34	2.06	–
J1133–6250	11:33:51.3(1)	–62:50:51(1)	0.9776360471(+6, –4)	–0.448(+9, –1)	(+132.0, –20.1)	128	1.22	–
J1136+1551	11:36:03.0946(5)	+15:51:15.9(1)	0.841809871701(+6, –2)	–2.64185(+9, –3)	(+0.34, –0.09)	36	3.63	–

Table A1 – continued

PSRJ	RAJ (hh:mm:ss)	DECJ (°:′:″)	ν (Hz)	$\dot{\nu}$ (10^{-15} s $^{-2}$)	$\ddot{\nu}$ (10^{-24} s $^{-3}$)	N_{ToA}	T (yr)	Flags
J1136–5525	11:36:02.2354(5)	–55:25:06.843(5)	2.74188009799(+1, –2)	–61.8(+1, –8)	(+0.6, –3.7)	147	3.53	–
J1141–3322	11:41:42.756(2)	–33:22:37.31(5)	3.43091071248(±3)	–5.4774(±1)	(+0.24, –0.14)	51	3.13	–
J1141–6545	11:41:07.0006(6)	–65:45:19.05(3)	2.53871590079(+6, –7)	–27.7621(±4)	0.48^{+7}_{-3}	273	3.55	B
J1146–6030	11:46:07.7152(1)	–60:30:59.622(9)	3.65798554138(±1)	–23.93026(±4)	(+0.53, –0.3)	169	3.35	–
J1157–6224	11:57:15.208(7)	–62:24:50.90(5)	2.49671858326(+9, –7)	–24.5068(+4, –5)	(+0.9, –0.63)	229	3.55	–
J1202–5820	12:02:28.358(6)	–58:20:33.41(5)	2.20846545731(+7, –6)	–10.3828(±3)	(+0.95, –0.6)	134	3.51	–
J1210–5559	12:10:05.98706(2)	–55:59:03.8501(2)	3.57439188715(±5)	–9.26691(+2, –3)	(+0.032, –0.003)	158	3.51	–
J1224–6407	12:24:22.264(2)	–64:07:53.79(1)	4.61934676092(+4, –5)	–105.6992(+3, –2)	(+0.09, –0.92)	367	3.55	–
J1231–6303	12:31:13.0(1)	–63:03:18(1)	0.74006295676(±3)	–0.0723(+8, –7)	(+2.4, –0.8)	79	3.38	–
J1239–6832	12:39:58.96(2)	–68:32:28.94(9)	0.768094857398(±2)	–7.01054(+7, –8)	(+1.1, –0.9)	60	3.15	–
J1243–6423	12:43:17.120(6)	–64:23:23.92(4)	2.57410111798(±5)	–29.8026(±3)	(+0.0, –0.49)	345	3.63	–
J1253–5820	12:53:28.418(2)	–58:20:40.47(2)	3.91392670035(±7)	–32.2492(±3)	(+1.24, –0.01)	204	3.38	–
J1257–1027	12:57:04.7796(9)	–10:27:04.77(3)	1.61993710136(+2, –1)	–0.94879(±4)	(+0.27, –0.39)	39	3.18	–
J1259–6741	12:59:22.64(1)	–67:41:40.27(6)	1.5075450023(+5, –4)	–1.9434(±1)	(+0.8, –1.6)	42	2.54	–
J1305–6455	13:05:23.47(2)	–64:55:28.5(1)	1.74931666048(+1, –2)	–12.3373(+9, –8)	(+1.2, –2.7)	175	3.47	–
J1306–6617	13:06:38.12(1)	–66:17:21.2(1)	2.11404065516(±2)	–26.7181(±9)	(+1.41, –0.41)	125	3.38	–
J1312–5402	13:12:04.708(2)	–54:02:42.5(2)	1.37333511678(+4, –5)	–0.2765(+2, –1)	(+0.7, –1.03)	36	3.18	–
J1312–5516	13:12:53.533(9)	–55:16:47.3(1)	1.1775198318(±3)	–7.9101(±1)	(+0.3, –0.99)	98	3.07	–
J1319–6056	13:19:20.250(7)	–60:56:46.79(6)	3.51675963943(+2, –9)	–18.8878(+3, –7)	(+0.87, –0.14)	199	3.19	–
J1320–5359	13:20:53.932(2)	–53:59:04.967(3)	3.57477758551(±6)	–118.146(±3)	0.36^{+1}_{-3}	129	3.5	–
J1326–5859	13:26:58.219(7)	–58:59:29.29(7)	2.09207813232(+7, –8)	–14.2359(+5, –4)	(+1.4, –1.0)	306	3.63	–
J1326–6408	13:26:32.433(2)	–64:08:43.80(1)	1.26155286486(+9, –6)	–4.91831(±2)	(+0.122, –0.15)	161	2.85	–
J1326–6700	13:26:02.706(4)	–67:00:50.1(3)	1.84156958655(+4, –3)	–18.037(±2)	(+1.3, –4.2)	132	3.54	–
J1327–6222	13:27:17.36(7)	–62:22:44.7(5)	1.8870445541(+4, –3)	–66.926(±2)	2.37^{+7}_{-5}	308	3.63	–
J1327–6301	13:27:07.4320(3)	–63:01:15.51(2)	5.08957797539(±4)	–39.6313(±1)	(+0.49, –0.29)	238	3.41	–
J1328–4357	13:28:06.4198(5)	–43:57:44.50(8)	1.87722052793(±7)	–10.7557(+4, –3)	0.29 ± 2	93	2.99	–
J1338–6204	13:38:09.247(7)	–62:04:18.7(5)	0.80710212469(±2)	–8.9837(+6, –5)	(+2.9, –4.5)	198	2.47	–
J1350–5115	13:50:16.159(2)	–51:15:24.56(3)	3.38180924275(+8, –6)	–8.6634(+2, –1)	(+4.0, –5.1)	95	2.43	–
J1355–5153	13:55:58.692(2)	–51:53:53.95(2)	1.55206115637(±3)	–6.7736(±1)	(+0.26, –0.23)	123	3.19	–
J1356–5521	13:56:50.49(2)	–55:21:15.2(2)	1.97090897627(±2)	–2.8152(+5, –4)	(+14.3, –9.1)	31	2.39	–

Table A1 – continued

PSRJ	RAJ (hh:mm:ss)	DECJ (°:′:″)	ν (Hz)	$\dot{\nu}$ (10^{-15} s^{-2})	$\ddot{\nu}$ (10^{-24} s^{-3})	N_{ToA}	T (yr)	Flags
J1359–6038	13:59:58.230(9)	–60:38:07.671(7)	7.84261649234(± 2)	–389.488(± 1)	–3 $^{+3.3}_{-1.1}$	429	3.54	–
J1401–6357	14:01:52.45(1)	–63:57:42.0(1)	1.18651362793(+8, –1)	–23.6871(+5, –4)	(+0.4, –1.3)	245	3.56	–
J1413–6307	14:13:31.32(4)	–63:07:34.6(3)	2.5319550816(± 1)	–47.9(+4, –3)	–4 $^{+3.3}_{-11.1}$	152	2.43	–
J1418–3921	14:18:50.28(1)	–39:21:18.6(2)	0.911737714389(+2, –3)	–0.73841(+8, –6)	(+0.42, –0.39)	57	3.63	–
J1420–5416	14:20:29.11(1)	–54:16:22.7(1)	1.06863614348(± 2)	–0.26515(+6, –7)	(+0.22, –0.3)	74	3.08	–
J1424–5822	14:24:32.130(8)	–58:22:55.7(1)	2.7267557238(+1, –9)	–29.262(± 2)	(+120.5, –91.9)	188	1.25	–
J1428–5530	14:28:26.240(3)	–55:30:50.06(4)	1.75348642691(± 1)	–6.41562(+4, –3)	0.055 \pm 5	168	3.66	–
J1430–6623	14:30:40.732(1)	–66:23:05.546(1)	1.2731663027(± 6)	–4.50256(+4, –3)	(+0.032, –0.039)	170	3.57	–
J1435–5954	14:35:00.208(1)	–59:54:49.5(1)	2.11418109778(± 4)	–6.9189(± 1)	(+0.81, –0.52)	254	3.49	–
J1452–6036	14:52:51.80(1)	–60:36:30.00(8)	6.4519415824(± 1)	–60.401(+3, –2)	(+105.1, –110.5)	152	1.32	–
J1453–6413	14:53:32.652(1)	–64:13:16.095(9)	5.571424352(+2, –3)	–85.1854(+2, –1)	(+0.18, –0.24)	234	3.56	–
J1456–6843	14:55:59.914(1)	–68:43:39.49(1)	3.79684009011(+5, –6)	–1.42687(+3, –2)	(+0.044, –0.009)	119	4.21	–
J1457–5122	14:57:40.093(8)	–51:22:54.9(1)	0.57198175779(+1, –2)	–1.73305(+5, –7)	(+0.22, –0.24)	39	3.03	–
J1507–4352	15:07:34.175(4)	–43:52:04.05(1)	3.48725495693(± 1)	–19.2672(+5, –4)	(+0.8, –1.4)	56	3.17	–
J1507–6640	15:07:48.634(1)	–66:40:57.86(1)	2.81170331276(+8, –9)	–9.1066(± 2)	(+0.22, –0.14)	111	2.97	–
J1511–5414	15:11:51.285(3)	–54:14:40.32(6)	4.99041973147(+8, –6)	–12.072(+1, –2)	(+144.8, –15.3)	101	1.25	–
J1512–5759	15:12:43.13(1)	–58:00:00.43(1)	7.77001479211(± 5)	–413.71(± 2)	(+1.7, –13.0)	177	3.19	–
J1514–4834	15:14:14.563(2)	–48:34:19.97(4)	2.19857371563(± 3)	–4.47652(+9, –8)	(+2.2, –0.3)	51	2.55	–
J1522–5829	15:22:42.244(4)	–58:29:02.815(3)	2.52937565301(+7, –9)	–13.1588(+3, –4)	(+0.25, –1.07)	187	3.21	–
J1527–3931	15:27:58.828(9)	–39:31:34.2(2)	0.41363243246(± 1)	–3.26122(+4, –5)	(+0.19, –0.15)	36	3.21	–
J1527–5552	15:27:40.734(4)	–55:52:08.352(6)	0.953544682096(+3, –4)	–10.2459(+2, –1)	(+0.25, –0.0)	134	3.21	–
J1528–3146	15:28:34.952(1)	–31:46:06.944(6)	16.4413569253(+2, –1)	–0.068(+5, –6)	(+1.36, –0.57)	25	3.05	B
J1534–5334	15:34:08.2790(1)	–53:34:19.57(2)	0.730523027415(+2, –3)	–0.76251(± 7)	(+0.013, –0.016)	231	3.63	–
J1534–5405	15:34:33.59(1)	–54:05:40.5(2)	3.4519643055(+1, –8)	–18.528(+2, –3)	4 $^{+5.5}_{-4.5}$	100	2.43	–
J1539–5626	15:39:14.07(1)	–56:26:26.2(1)	4.10852985562(+3, –6)	–81.894(+3, –1)	(+1.5, –7.0)	179	3.13	–
J1542–5034	15:42:45.32(2)	–50:34:03.66(3)	1.6687581689(+9, –1)	–11.208(+4, –3)	(+5.2, –7.3)	59	2.39	–
J1543+0929	15:43:38.82(2)	+09:29:16.4(5)	1.33609682985(± 2)	–0.7773(± 7)	(+1.7, –1.6)	28	2.75	–
J1544–5308	15:44:59.8294(6)	–53:08:46.953(9)	5.60055059845(+1, –9)	–1.88991(+3, –4)	(+0.17, –0.26)	164	3.58	–
J1549–4848	15:49:21.027(6)	–48:48:36.1(1)	3.46791653545(+9, –1)	–169.702(± 2)	(+63.2, –56.4)	44	1.46	–
J1553–5456	15:53:59.61(1)	–54:56:06.25(1)	0.9247724034(+6, –5)	–13.4399(± 1)	(+36.6, –44.9)	73	1.21	–

Table A1 – continued

PSRJ	RAJ (hh:mm:ss)	DECJ (°:′:″)	ν (Hz)	$\dot{\nu}$ (10^{-15} s^{-2})	$\ddot{\nu}$ (10^{-24} s^{-3})	N_{ToA}	T (yr)	Flags
J1555–3134	15:55:17.947(2)	–31:34:20.3(1)	1.93009273101(±2)	–0.23061(±7)	(+0.34, –0.11)	49	3.19	–
J1557–4258	15:57:00.25445(6)	–42:58:12.35(1)	3.0377858242(+1, –2)	–3.04646(+8, –7)	(+0.05, –0.131)	90	3.54	–
J1559–4438	15:59:41.525(1)	–44:38:45.85(3)	3.89018703598(+2, –3)	–15.4484(±2)	(+0.53, –0.27)	66	3.37	–
J1559–5545	15:59:20.7(1)	–55:45:47(1)	1.04464080328(±5)	–21.733(±3)	(+12.5, –3.9)	87	3.49	–
J1600–3053	16:00:51.8941(7)	–30:53:49.70(3)	277.937706823(±2)	–0.687(±5)	(+47.9, –46.2)	32	3.39	PPTA, B
J1600–5044	16:00:53.033(5)	–50:44:20.93(8)	5.19197591119(±2)	–136.452(+1, –9)	(+3.1, –1.2)	175	3.63	–
J1603–2531	16:03:04.8253(6)	–25:31:47.9(4)	3.53267858106(±4)	–19.8906(±2)	(+1.13, –0.29)	29	3.36	–
J1603–2712	16:03:08.036(1)	–27:13:27.0(7)	1.28482652061(±4)	–4.9683(+1, –2)	(+0.11, –0.28)	29	3.0	–
J1603–7202	16:03:35.6736(9)	–72:02:32.795(7)	67.3765811129(+1, –2)	–0.074(+6, –5)	(+0.66, –0.56)	38	3.11	PPTA, B
J1604–4909	16:04:22.985(2)	–49:09:58.33(5)	3.05419496456(±5)	–9.4894(±3)	(+1.25, –0.25)	113	3.47	–
J1605–5257	16:05:16.265(3)	–52:57:34.80(5)	1.51972586121(±1)	–0.59109(+4, –3)	(+0.12, –0.43)	162	3.75	–
J1613–4714	16:13:29.018(4)	–47:14:26.41(8)	2.61522196138(±2)	–4.33493(±6)	(+0.31, –0.23)	65	3.35	–
J1622–4950	16:22:44.80(3)	–49:50:54.5(5)	0.2311087(±3)	–526(+54.3, –56.9)	(+5145.6, –7084.3)	77	1.21	–
J1623–0908	16:23:17.658(4)	–09:08:48.9(3)	0.783424111867(+2, –1)	–1.58401(±5)	(+0.36, –0.49)	31	3.13	–
J1623–4256	16:23:48.291(6)	–42:56:52.6(1)	2.74279572052(±1)	–7.5624(+8, –7)	(+1.16, –0.06)	57	3.47	–
J1626–4537	16:26:48.94(1)	–45:37:25.8(6)	2.701641249(±2)	–60.541(±4)	(+190.9, –230.7)	35	1.21	–
J1633–4453	16:33:47.03(3)	–44:53:08.58(7)	2.2908895877(±3)	–32.539(+5, –6)	(+327.5, –153.7)	33	1.24	–
J1633–5015	16:33:00.0861(1)	–50:15:08.358(3)	2.83973605453(±1)	–30.54746(±4)	(+0.128, –0.07)	110	3.74	–
J1639–4604	16:39:21.198(3)	–46:04:33.23(7)	1.88992880367(±3)	–20.60947(±9)	(+0.69, –0.88)	57	2.47	–
J1644–4559	16:44:49.234(6)	–45:59:10.3(1)	2.19742452445(+4, –3)	–96.9653(+4, –5)	$1_{-1.4}^{+1.1}$	648	4.1	–
J1646–6831	16:46:54.91(3)	–68:31:51.7(1)	0.560031669373(±2)	–0.5337(±1)	(+0.074, –0.14)	27	3.35	–
J1651–4246	16:51:48.797(6)	–42:46:09.97(1)	1.18472094037(+4, –5)	–6.662(+3, –2)	(+0.72, –0.76)	148	3.46	–
J1651–5222	16:51:42.962(2)	–52:22:58.38(3)	1.5746588888(±1)	–4.48968(±3)	(+0.24, –0.017)	95	3.38	–
J1651–5255	16:51:41.41(1)	–52:55:47.7(2)	1.12291858733(±1)	–2.6677(±6)	(+0.94, –0.04)	71	3.14	–
J1652–2404	16:52:58.50(5)	–24:03:54(7)	0.586943472123(+4, –3)	–1.0877(±1)	(+0.29, –0.26)	27	2.87	–
J1700–3312	17:00:52.96(2)	–33:12:45(1)	0.736209097583(+6, –5)	–2.5543(±2)	(+0.19, –0.37)	53	3.36	–
J1701–3726	17:01:18.45(1)	–37:26:27.2(5)	0.407395359535(±2)	–1.84611(+5, –6)	(+0.23, –0.21)	62	3.17	–
J1703–1846	17:03:51.102(9)	–18:46:13(1)	1.24325189271(±3)	–2.67613(±1)	(+0.06, –0.21)	34	3.18	–
J1703–3241	17:03:22.514(2)	–32:41:48.5(1)	0.825228539025(±5)	–0.44787(±2)	(+0.057, –0.067)	81	3.54	–
J1703–4851	17:03:54.541(7)	–48:52:01.04(1)	0.716124628374(±2)	–2.60178(+5, –7)	(+0.22, –0.09)	50	3.36	–

Table A1 – continued

PSRJ	RAJ (hh:mm:ss)	DECJ (°:′:″)	ν (Hz)	$\dot{\nu}$ (10^{-15} s^{-2})	$\ddot{\nu}$ (10^{-24} s^{-3})	N_{ToA}	T (yr)	Flags
J1705–1906	17:05:36.093(2)	–19:06:39.2(3)	3.34458679304(+6, –7)	–46.2498(±3)	(+0.27, –0.89)	78	3.52	–
J1705–3423	17:05:42.362(3)	–34:23:43.1(2)	3.91501633777(±1)	–16.4861(+6, –5)	(+0.6, –1.6)	112	3.43	–
J1707–4053	17:07:21.78(2)	–40:53:55.1(9)	1.72111797519(±2)	–5.6882(+5, –4)	(+2.0, –1.5)	57	3.51	–
J1708–3426	17:08:57.79(1)	–34:26:44.0(6)	1.44484514046(+3, –5)	–8.7827(±2)	(+0.42, –0.59)	52	3.35	–
J1709–1640	17:09:26.452(4)	–16:40:59.2(4)	1.53125350203(+1, –7)	–14.8003(+5, –6)	0.61 ± 2	38	3.63	–
J1709–4429	17:09:42.62(5)	–44:29:12(1)	9.7542901224(+6, –4)	–8850.16(+6, –8)	196 $^{+31.4}_{-20.1}$	111	3.5	–
J1711–5350	17:11:53.13(1)	–53:50:18.3(2)	1.11205916031(±1)	–19.2133(±5)	(+0.47, –0.73)	46	3.1	–
J1715–4034	17:15:40.92(3)	–40:34:18(1)	0.482589475307(+7, –6)	–0.7063(±2)	(+0.48, –0.52)	76	3.5	–
J1717–3425	17:17:20.30(1)	–34:25:00.31(8)	1.52368077976(+5, –6)	–22.72(±2)	2 $^{+1.7}_{-1.6}$	56	2.38	–
J1717–4054	17:17:52.31(1)	–41:03:13.0(4)	1.12648202933(+6, –8)	–4.7161(+8, –5)	–1.54 $^{+9}_{-2}$	31	4.09	–
J1720–1633	17:20:25.23(1)	–16:33:35(1)	0.638730665146(±3)	–2.3719(+9, –1)	(+0.23, –0.06)	41	3.13	–
J1720–2933	17:20:34.131(5)	–29:33:14.0(5)	1.61173637049(+3, –2)	–1.9396(±1)	(+0.22, –0.22)	43	3.29	–
J1722–3207	17:22:02.9641(1)	–32:07:45.07(6)	2.09574210095(±3)	–2.8316(±1)	(+0.2, –0.22)	89	3.17	–
J1722–3712	17:22:59.17(5)	–37:12:03.(2)	4.23402576366(±4)	–194.486(±2)	16 $^{+13.7}_{-12.7}$	116	3.1	–
J1727–2739	17:27:30.98(3)	–27:38:53(4)	0.7733354277(+3, –2)	–0.6399(+5, –6)	3 $^{+15.8}_{-1.7}$	34	2.42	–
J1730–2304	17:30:21.682(4)	–23:04:30(1)	123.110287079(+1, –9)	–0.3023(+2, –4)	(+1.6, –1.2)	42	3.3	PPTA
J1731–4744	17:31:42.21(1)	–47:44:38.7(4)	1.2049313854(+2, –3)	–237.394(±5)	–9 $^{+3.2}_{-0.6}$	145	3.58	–
J1733–2228	17:33:26.43(3)	–22:28:37(10)	1.14720621377(±5)	–0.0585(+2, –1)	23 $^{+0.0}_{-14.1}$	40	3.05	–
J1736–2457	17:36:45.4(1)	–24:57:50(33)	0.3784689286(+3, –2)	–0.452(+5, –6)	(+174.6, –205.3)	25	1.14	–
J1739–2903	17:39:34.285(2)	–29:03:03.96(3)	3.09704932896(+9, –8)	–75.5355(+3, –4)	(+0.36, –0.6)	88	3.02	–
J1740–3015	17:40:33.98(5)	–30:15:22(5)	1.647450502(+2, –3)	–1263.51(+7, –9)	(+46.0, –51.7)	229	3.47	–
J1741–3927	17:41:18.079(1)	–39:27:38.12(7)	1.95231526583(±1)	–6.4645(+5, –6)	2.81 $^{+3}_{-5}$	74	3.14	–
J1743–3150	17:43:36.710(8)	–31:50:22.7(9)	0.414138298084(±1)	–20.7152(+4, –5)	(+0.13, –0.09)	84	3.16	–
J1745–3040	17:45:56.3081(6)	–30:40:23.30(6)	2.72156341619(+1, –2)	–79.04005(+8, –9)	(+0.23, –0.1)	110	3.5	–
J1751–4657	17:51:42.185(1)	–46:57:26.72(4)	1.34706694407(+4, –3)	–2.35478(+1, –2)	(+0.09, –0.083)	53	3.61	–
J1752–2806	17:52:58.707(8)	–28:06:36(1)	1.77757096075(±6)	–25.6877(+8, –7)	0.51 $^{+3}_{-4}$	145	4.1	–
J1757–2421	17:57:29.37(1)	–24:19:54(10)	4.2715099866(+2, –3)	–236.544(+5, –4)	(+166.8, –147.0)	66	1.31	–
J1759–2205	17:59:24.164(4)	–22:05:33(2)	2.16928428064(+1, –2)	–51.0746(+7, –6)	(+1.52, –0.26)	54	3.02	–
J1759–3107	17:59:22.056(4)	–31:07:21.8(5)	0.926822758345(±3)	–3.24135(±9)	(+0.81, –0.48)	40	2.39	–
J1801–0357	18:01:22.628(3)	–03:57:55.7(2)	1.08519559579(±4)	–3.8928(±1)	(+0.78, –0.46)	29	2.34	–

Table A1 – continued

PSRJ	RAJ (hh:mm:ss)	DECJ (°:′:″)	ν (Hz)	$\dot{\nu}$ (10^{-15} s^{-2})	$\ddot{\nu}$ (10^{-24} s^{-3})	N_{ToA}	T (yr)	Flags
J1801–2920	18:01:46.839(3)	–29:20:38.1(3)	0.924290873961(± 1)	–2.81266(± 3)	(+0.24, –0.02)	60	3.26	–
J1803–2137	18:03:51.4(1)	–21:37:07.(27)	7.478883401(+4, –6)	–7488(+1.1, –0.9)	$283_{-39.6}^{+29.1}$	52	1.29	–
J1805–1504	18:05:06.1(2)	–15:04:36(10)	0.84654711(± 1)	–0.31(± 2)	(+378.9, –625.7)	28	1.25	–
J1807–0847	18:07:38.0259(2)	–08:47:43.28(1)	6.10771328217(+6, –5)	–1.06808(+2, –1)	(+0.12, –0.057)	74	3.7	–
J1807–2715	18:07:08.4918(3)	–27:15:02.07(5)	1.20804374592(± 6)	–17.8128(± 2)	(+0.65, –0.2)	77	3.12	–
J1808–0813	18:08:09.432(1)	–08:13:01.8(4)	1.14149384538(± 5)	–1.6108(± 2)	(+0.13, –0.35)	32	3.38	–
J1809–2109	18:09:14.32(3)	–21:09:02.(5)	1.42365721129(± 4)	–7.747(± 1)	(+22.7, –13.0)	29	2.4	–
J1810–5338	18:10:44.473(3)	–53:38:07.631(6)	3.8306868647(± 4)	–5.6604(± 1)	(+0.78, –0.49)	32	2.96	–
J1816–2650	18:16:35.399(6)	–26:49:53(1)	1.68666719259(+2, –3)	–0.18919(+9, –1)	(+0.75, –0.83)	51	3.35	–
J1818–1422	18:18:23.77(1)	–14:22:39(1)	3.43064845763(± 2)	–23.9924(+6, –7)	(+1.2, –3.0)	51	3.02	–
J1820–0427	18:20:52.559(2)	–04:27:37.9(1)	1.67201171071(+6, –9)	–17.6967(+5, –3)	-0.64_{-6}^{+5}	55	3.63	–
J1822–2256	18:22:58.95(4)	–22:56:29(16)	0.53354117731(± 2)	–0.38531(± 5)	(+0.31, –0.14)	57	3.33	–
J1823–0154	18:23:52.138(3)	–01:54:04.94(1)	1.31617369972(+3, –2)	–1.95718(± 9)	(+0.41, –0.34)	35	3.14	–
J1823–1115	18:23:40.3(1)	–11:15:11(1)	3.57360247363(± 2)	–17.5869(+7, –8)	(+2.8, –2.4)	53	3.19	B
J1823–3106	18:23:46.819(4)	–31:06:48.0(3)	3.52042950493(+1, –9)	–36.3594(+4, –6)	0.69 ± 3	35	3.11	–
J1824–0127	18:24:53.43(1)	–01:27:51.4(4)	0.400084842618(± 3)	–0.62531(+8, –1)	(+0.81, –0.82)	30	2.4	–
J1824–1945	18:24:00.4360(4)	–19:45:44.5(8)	5.28154642765(± 1)	–146.2029(+8, –7)	$-2_{-1.9}^{+1.9}$	95	3.38	–
J1825–0935	18:25:30.62(6)	–09:35:22(4)	1.3003801253(± 1)	–88.397(± 3)	(+59.4, –52.1)	144	3.84	–
J1827–0750	18:27:02.7071(6)	–07:50:15.4(2)	3.69682174881(+6, –5)	–21.224(± 2)	(+8.0, –6.7)	49	2.36	–
J1829–1751	18:29:43.15(1)	–17:51:13(1)	3.25587939511(+2, –3)	–58.78(± 1)	(+0.9, –1.1)	79	3.41	–
J1830–1135	18:30:01.787(6)	–11:35:27(6)	0.160730937421(± 6)	–1.2319(± 2)	(+0.51, –0.61)	40	2.99	–
J1832–0827	18:32:37.013(2)	–08:27:03.16(1)	1.54478860938(± 6)	–152.4959(+3, –2)	-0.39 ± 3	93	3.21	–
J1833–0338	18:33:42.028(8)	–03:39:08.00(3)	1.45617035595(+1, –9)	–88.0832(+4, –5)	$1_{-1.7}^{+1.1}$	102	3.19	–
J1833–0827	18:33:40.245(2)	–08:27:30.9(1)	11.7247184586(± 5)	–1261.993(± 2)	(+4.1, –5.2)	54	2.96	–
J1834–0426	18:34:25.621(3)	–04:26:15.7(2)	3.44698922332(± 3)	–0.8605(± 1)	(+1.0, –0.8)	53	3.22	–
J1835–1020	18:35:57.44(3)	–10:19:51(2)	3.3063181115(± 1)	–64.651(± 5)	(+5.2, –16.0)	53	3.23	–
J1836–0436	18:36:51.77(1)	–04:36:37.3(7)	2.82296346028(± 4)	–13.232(± 1)	(+11.7, –48.8)	31	2.42	–
J1836–1008	18:36:53.922(3)	–10:08:09.39(2)	1.77708391524(+8, –1)	–37.1805(+8, –4)	(+1.2, –1.3)	74	3.53	–
J1837–0653	18:37:14.53(7)	–06:52:55(5)	0.52471147608(+4, –5)	–0.194(+2, –1)	(+6.1, –6.1)	50	2.24	–
J1840–0809	18:40:33.365(6)	–08:09:03.62(4)	1.04638272527(± 3)	–2.57306(+9, –1)	(+0.17, –0.2)	75	3.43	–

Table A1 – continued

PSRJ	RAJ (hh:mm:ss)	DECJ (°:′:″)	ν (Hz)	$\dot{\nu}$ (10^{-15} s^{-2})	$\ddot{\nu}$ (10^{-24} s^{-3})	N_{ToA}	T (yr)	Flags
J1840–0815	18:40:13.756(9)	–08:15:08.88(4)	0.912041662037(± 3)	–2.01835(± 8)	(+0.6, –1.3)	51	2.44	–
J1841–0425	18:41:05.663(5)	–04:25:19.5(2)	5.37198570613(± 4)	–184.318(± 1)	(+3.2, –6.3)	31	2.24	–
J1841+0912	18:41:55.921(7)	+09:12:07.29(2)	2.62246808546(+3, –4)	–7.505(+2, –1)	(+0.3, –4.2)	29	3.23	–
J1842–0359	18:42:26.49(1)	–04:00:01.52(7)	0.543494594895(± 5)	–0.1501(± 1)	(+0.4, –1.0)	77	3.44	–
J1843–0000	18:43:27.965(9)	–00:00:41.5(2)	1.13593208324(+1, –2)	–10.0305(± 7)	(+1.0, –0.7)	60	3.19	–
J1844–0433	18:44:33.446(3)	–04:33:12.5(1)	1.00905187281(± 2)	–3.98545(+4, –5)	(+0.29, –0.24)	46	2.68	–
J1845–0743	18:45:57.1763(9)	–07:43:38.16(5)	9.55157970586(+5, –4)	–33.444(± 1)	(+1.5, –2.4)	72	2.46	–
J1847–0402	18:47:22.850(1)	–04:02:14.70(7)	1.67277577163(+6, –4)	–144.6391(+2, –3)	(+0.36, –0.0)	127	3.53	–
J1848–0123	18:48:23.596(1)	–01:23:58.48(6)	1.51644857592(+3, –6)	–11.9808(+4, –2)	0.19_{-1}^{+2}	111	3.49	–
J1849–0636	18:49:06.4647(2)	–06:37:06.91(1)	0.689011346415(± 3)	–21.9601(± 1)	(+0.02, –0.23)	108	3.23	–
J1852–0635	18:52:57.448(5)	–06:36:00.45(2)	1.90782618111(+5, –4)	–53.2438(± 1)	(+0.59, –0.23)	109	3.25	–
J1852–2610	18:52:59.471(5)	–26:10:13.6(6)	2.9732067598(± 6)	–0.7704(+1, –2)	(+1.5, –1.9)	25	2.43	–
J1857+0212	18:57:43.654(8)	+02:12:41.0(3)	2.40470716439(+9, –1)	–232.7342(± 3)	(+1.4, –0.35)	71	2.72	–
J1900–2600	19:00:47.542(5)	–26:00:44.8(6)	1.63342812459(± 1)	–0.54862(+4, –5)	(+0.15, –0.167)	40	3.44	–
J1901+0331	19:01:31.76(1)	+03:31:06.73(4)	1.52565744968(± 2)	–17.3341(+8, –6)	(+2.3, –2.6)	127	3.13	–
J1901+0716	19:01:39.02(1)	+07:16:33.6(5)	1.55279458439(± 4)	–5.577(± 1)	(+4.6, –1.3)	28	2.61	–
J1901–0906	19:01:53.007(3)	–09:06:10.9(2)	0.561189668479(+6, –7)	–0.516(± 2)	(+0.08, –0.19)	52	3.12	–
J1902+0556	19:02:42.60(1)	+05:56:25.8(1)	1.33943019014(± 1)	–23.0839(± 4)	(+1.3, –2.6)	32	2.44	–
J1902+0615	19:02:50.277(3)	+06:16:33.41(7)	1.48476895959(± 4)	–16.9975(± 1)	(+0.5, –2.3)	45	2.62	–
J1903+0135	19:03:29.973(1)	+01:35:38.73(4)	1.37116475483(± 2)	–7.57312(± 8)	(+0.16, –0.28)	94	3.18	–
J1903–0632	19:03:37.934(2)	–06:32:21.52(9)	2.31540809127(+7, –8)	–18.1244(+4, –3)	(+0.16, –0.71)	69	3.14	–
J1905–0056	19:05:27.752(6)	–00:56:40.8(3)	1.55476661905(+7, –6)	–7.3951(± 1)	(+2.0, –1.7)	29	2.45	–
J1909+0007	19:09:35.252(2)	+00:07:56.84(9)	0.983329997648(+4, –7)	–5.3391(+3, –2)	(+0.37, –0.68)	71	3.07	–
J1909+0254	19:09:38.311(2)	+02:54:50.36(9)	1.01026940483(± 1)	–5.61185(± 4)	(+0.24, –0.1)	51	3.19	–
J1909+1102	19:09:48.6829(9)	+11:02:03.044(3)	3.5255695764(+1, –9)	–32.8178(± 4)	$1_{-1.1}^{+0.7}$	95	3.19	–
J1909–3744	19:09:47.42783(7)	–37:44:14.767(3)	339.315686856(± 5)	–1.6153(± 2)	(+4, –5)	68	3.54	PPTA, B
J1910–0309	19:10:29.692(2)	–03:09:54.1(1)	1.98174395507(+3, –4)	–8.61183(± 1)	-0.22_{-4}^{+2}	43	3.09	–
J1910+0358	19:10:09.016(3)	+03:58:30(1)	0.429135601854(+1, –8)	–0.8134(± 3)	(+1.6, –1.9)	44	2.39	–
J1913–0440	19:13:54.1624(9)	–04:40:47.56(4)	1.21074218559(± 2)	–5.9681(± 1)	(+0.38, –0.21)	88	3.52	–
J1913+1400	19:13:24.352(1)	+14:00:52.50(3)	1.91764388163(+2, –3)	–2.95953(± 7)	(+0.29, –0.24)	66	2.63	–

Table A1 – continued

PSRJ	RAJ (hh:mm:ss)	DECJ (°:′:″)	ν (Hz)	$\dot{\nu}$ (10^{-15} s^{-2})	$\ddot{\nu}$ (10^{-24} s^{-3})	N_{ToA}	T (yr)	Flags
J1915+1009	19:15:29.993(1)	+10:09:43.58(3)	2.47187153893(±3)	−93.22115(+9, −8)	(+0.71, −0.2)	105	3.13	–
J1916+0951	19:16:32.333(1)	+09:51:25.97(3)	3.70019376623(±8)	−34.52(+4, −3)	(+0.1, −0.51)	86	3.17	–
J1916+1312	19:16:58.67(2)	+13:12:50.0(4)	3.548050079(±2)	−46.069(+4, −5)	(+49.9, −9.6)	39	161.67	–
J1917+1353	19:17:39.794(3)	+13:53:57.16(8)	5.13779943103(±4)	−189.936(±1)	$1_{-1.5}^{+1.1}$	71	2.47	–
J1919+0021	19:19:50.670(2)	+00:21:39.8(1)	0.78599927(+8, −7)	−4.74138(+2, −3)	(+0.18, −0.15)	97	3.26	–
J1926+0431	19:26:24.472(2)	+04:31:31.54(8)	0.931029279866(+1, −2)	−2.13409(+4, −5)	(+0.18, −0.1)	130	3.18	–
J1932+1059	19:32:14.038(2)	+10:59:33.21(5)	4.41464565156(±1)	−22.5369(+7, −6)	(+1.6, −1.4)	116	3.64	–
J1932−3655	19:32:06.1280(6)	−36:55:01.78(3)	1.75002463079(+9, −1)	−0.8767(±3)	(+0.6, −3.6)	39	2.38	–
J1935+1616	19:35:47.8255(2)	+16:16:39.723(4)	2.78750145981(+3, −5)	−46.6373(+1, −8)	(+0.51, −0.31)	59	2.15	–
J1941−2602	19:41:00.4169(1)	−26:02:05.884(9)	2.48226091399(+9, −8)	−5.89424(±2)	(+0.21, −0.098)	105	3.09	–
J1943−1237	19:43:25.461(3)	−12:37:42.9(2)	1.02835150982(+1, −9)	−1.75624(+4, −3)	(+1.4, −0.2)	54	3.22	–
J1945−0040	19:45:28.33(3)	−00:40:59(1)	0.9563585837(±1)	−0.47(±2)	(+79.1, −88.5)	64	1.3	–
J1946−2913	19:46:51.757(5)	−29:13:48.1(3)	1.04226478935(±1)	−1.61748(+5, −4)	(+0.2, −0.14)	63	3.27	–
J2006−0807	20:06:16.365(4)	−08:07:02.16(2)	1.72155151633(±5)	−0.1355(+1, −9)	(+0.52, −0.4)	255	3.42	–
J2033+0042	20:33:31.12(2)	+00:42:24.1(9)	0.199465428208(+3, −2)	−0.38564(+6, −7)	(+0.21, −0.09)	129	3.28	–
J2038−3816	20:38:54.36(3)	−38:16:15.6(9)	0.633999188596(±9)	−1.6728(±3)	(+2.6, −6.7)	48	2.4	–
J2046−0421	20:46:00.1760(2)	−04:21:26.3(1)	0.646437789195(+1, −9)	−0.61473(+3, −2)	(+0.044, −0.064)	141	3.41	–
J2046+1540	20:46:39.336(5)	+15:40:33.6(1)	0.878513972444(±3)	−0.14056(±7)	(+0.21, −0.24)	72	3.39	–
J2048−1616	20:48:35.74(2)	−16:16:45(1)	0.509792367545(±6)	−2.84929(±2)	(+0.071, −0.055)	105	4.04	–
J2051−0827	20:51:07.52058(5)	−08:27:37.61(2)	221.796283548(±3)	−0.6248(+9, −7)	(+2.6, −0.5)	193	3.23	B
J2053−7200	20:53:47.280(4)	−72:00:42.48(2)	2.9296611297(±3)	−1.69606(+9, −8)	(+0.1, −0.19)	64	3.22	–
J2116+1414	21:16:13.761(1)	+14:14:20.38(4)	2.27193569866(±4)	−1.49439(±8)	(+0.13, −0.38)	127	3.18	–
J2129−5721	21:29:22.77664(9)	−57:21:14.2954(7)	268.359226956(±2)	−1.5024(±5)	(+14.1, −15.3)	100	2.22	PPTA, B
J2144−3933	21:44:12.01(1)	−39:33:58.4(3)	0.117511188481(+4, −5)	−0.0064(+1, −2)	(+0.038, −0.089)	95	3.2	–
J2145−0750	21:45:50.4552(8)	−07:50:18.56(3)	62.2958878113(±3)	−0.111(±1)	(+2.5, −0.1)	162	3.12	PPTA, B
J2155−3118	21:55:13.64(1)	−31:18:53.8(2)	0.97087088287(+3, −2)	−1.16876(+7, −8)	(+0.25, −0.21)	61	3.08	–
J2222−0137	22:22:05.96713(1)	−01:37:15.731(5)	30.4712133291(±1)	−0.0535(+3, −5)	(+0.67, −0.17)	216	3.2	B
J2241−5236	22:41:42.03154(6)	−52:36:36.2491(6)	457.310149438(+9, −1)	−1.4408(±6)	(+0.65, −0.81)	295	3.27	PPTA, B
J2248−0101	22:48:26.884(6)	−01:01:48.0(2)	2.09541027394(±5)	−2.8961(±1)	(+0.8, −2.5)	172	2.54	–
J2324−6054	23:24:27.14(1)	−60:54:05.794(9)	0.425987202198(+1, −9)	−0.46843(+3, −4)	(+0.061, −0.12)	87	3.07	–

Table A1 – *continued*

PSRJ	RAJ (hh:mm:ss)	DECJ (°:′:″)	ν (Hz)	$\dot{\nu}$ (10^{-15} s^{-2})	$\ddot{\nu}$ (10^{-24} s^{-3})	N_{ToA}	T (yr)	Flags
J2330–2005	23:30:26.986(2)	–20:05:29.75(7)	0.608411174931(± 4)	–1.71419(± 1)	(+0.042, –0.097)	172	3.52	–
J2346–0609	23:46:50.54(1)	–06:10:01.04(4)	0.846407381972(± 3)	–0.9728(± 1)	(+0.04, –0.46)	236	3.23	–

APPENDIX B: TIMING NOISE PARAMETERS

Preferred models indicated are: white timing noise (WTN), power-law red noise (PLRN), power law red noise with low-frequency turnover (PL+FC) and power-law red noise with $\dot{\nu}$ (PLRN+F2). The listed Bayes factor is taken as being the difference in evidences between the best model and the next simplest model.

This paper has been typeset from a $\text{\TeX}/\text{\LaTeX}$ file prepared by the author.

Table B1. List of the preferred timing noise model, Bayes factor when compared to the next simplest model and associated red noise parameters (errors indicate the 95 percent confidence intervals) for each pulsar in our data set. MSPs are indicated by a \star and clock reference pulsars by a \dagger . The red noise of clock reference pulsars (such as PSR J0437–4715) are contaminated by residual clock jumps, so should be used with caution. The full table can be found in the supplementary material.

PSRJ	Model	$\ln(\mathcal{B})$	$\log_{10}(A)$ ($\text{yr}^{3/2}$)	β
J0030+0451 \star	WTN	–	–	–
J0134–2937	WTN	–	–	–
J0151–0635	WTN	–	–	–
J0152–1637	WTN	–	–	–
J0206–4028	WTN	–	–	–
J0255–5304	WTN	–	–	–
J0348+0432 \star	WTN	–	–	–
J0401–7608	PLRN	10.6	$-10.2^{+0.2}_{-0.5}$	$4.0^{+14.4}_{-2.5}$
J0418–4154	WTN	–	–	–
J0437–4715 $\star\dagger$	PLRN	4.2	$-10.8^{+0.7}_{-0.4}$	$9.5^{+3.8}_{-2.5}$
J0450–1248	WTN	–	–	–
J0452–1759	PLRN	22.0	$-10.4^{+0.3}_{-0.7}$	$3.1^{+3.5}_{-2.0}$
J0525+1115	WTN	–	–	–
J0529–6652	WTN	–	–	–
J0533+0402	WTN	–	–	–
J0536–7543	WTN	–	–	–
J0601–0527	WTN	–	–	–
J0624–0424	WTN	–	–	–
J0627+0706	PLRN	60.2	$-10.0^{+0.4}_{-0.4}$	$3.5^{+2.5}_{-1.7}$
J0630–2834	WTN	–	–	–
J0646+0905	WTN	–	–	–
J0659+1414	PLRN	26.8	$-10.1^{+0.4}_{-3.5}$	$5.6^{+14.3}_{-2.1}$
J0711–6830 \star	WTN	–	–	–
J0729–1836	PLRN	191.6	$-9.7^{+0.3}_{-0.3}$	$6.1^{+3.0}_{-2.0}$
J0737–3039A \star	WTN	–	–	–
J0738–4042	PLRN+F2	5.4	$-9.8^{+0.3}_{-0.2}$	$6.5^{+1.8}_{-1.4}$
J0742–2822	PLRN	512.3	$-9.0^{+0.2}_{-0.1}$	$4.8^{+1.4}_{-1.0}$
J0758–1528	PLRN	3.2	$-10.7^{+0.6}_{-3.9}$	$4.1^{+15.8}_{-1.8}$
J0809–4753	PLRN	3.5	$-11.1^{+1.2}_{-3.6}$	$5.7^{+14.2}_{-3.5}$
J0820–1350	WTN	–	–	–
J0820–4114	WTN	–	–	–
J0835–4510	PLRN	3173.2	$-8.2^{+0.2}_{-0.2}$	$8.6^{+0.9}_{-0.9}$
J0837+0610	WTN	–	–	–
J0837–4135	PLRN	138.6	$-11.7^{+0.8}_{-1.0}$	$7.5^{+5.5}_{-2.9}$
J0840–5332	WTN	–	–	–
J0842–4851	WTN	–	–	–
J0846–3533	WTN	–	–	–

Table B1 – continued

PSRJ	Model	$\ln(\mathcal{B})$	$\log_{10}(A)$ (yr ^{3/2})	β
J0855–3331	WTN	–	–	–
J0856–6137	WTN	–	–	–
J0904–4246	WTN	–	–	–
J0904–7459	WTN	–	–	–
J0907–5157	PLRN	92.7	$-10.8^{+0.7}_{-3.4}$	$5.8^{+14.2}_{-2.1}$
J0908–1739	WTN	–	–	–
J0908–4913	PLRN	523.7	$-9.6^{+0.2}_{-0.2}$	$5.0^{+1.0}_{-0.8}$
J0909–7212	WTN	–	–	–
J0922+0638	PLRN	101.1	$-9.4^{+0.2}_{-0.2}$	$5.6^{+1.8}_{-2.0}$
J0924–5302	PLRN	279.9	$-9.3^{+0.3}_{-0.2}$	$4.5^{+1.3}_{-1.1}$
J0924–5814	WTN	–	–	–
J0934–5249	WTN	–	–	–
J0942–5552	PLRN	523.1	$-9.0^{+0.2}_{-0.2}$	$5.9^{+1.6}_{-1.1}$
J0942–5657	PLRN	26.5	$-13.1^{+2.6}_{-1.0}$	$17.4^{+2.6}_{-11.6}$
J0944–1354	WTN	–	–	–
J0953+0755	WTN	–	–	–
J0955–5304	WTN	–	–	–
J0959–4809	WTN	–	–	–
J1001–5507	PLRN	492.9	$-9.1^{+0.2}_{-0.1}$	$4.6^{+1.2}_{-0.8}$
J1003–4747	WTN	–	–	–
J1012–5857	WTN	–	–	–
J1013–5934	WTN	–	–	–
J1016–5345	WTN	–	–	–
J1017–5621	WTN	–	–	–
J1017–7156*	WTN	–	–	–
J1022+1001*	WTN	–	–	–
J1032–5911	WTN	–	–	–
J1034–3224	WTN	–	–	–
J1036–4926	WTN	–	–	–
J1041–1942	WTN	–	–	–
J1042–5521	WTN	–	–	–
J1043–6116	WTN	–	–	–
J1045–4509*	WTN	–	–	–
J1046–5813	PLRN	7.0	$-13.2^{+2.9}_{-1.1}$	$18.3^{+1.6}_{-14.4}$
J1047–6709	WTN	–	–	–
J1048–5832	PLRN	1258.2	$-8.6^{+0.2}_{-0.1}$	$6.3^{+1.2}_{-1.0}$
J1056–6258	PLRN	297.3	$-9.7^{+0.2}_{-0.2}$	$2.9^{+1.1}_{-1.0}$
J1057–5226	PLRN	267.5	$-9.9^{+0.2}_{-0.2}$	$5.9^{+2.3}_{-1.5}$
J1057–7914	WTN	–	–	–
J1059–5742	WTN	–	–	–
J1105–6107	PLRN	347.5	$-8.9^{+0.3}_{-0.2}$	$4.1^{+1.7}_{-1.2}$

Table B1 – continued

PSRJ	Model	$\ln(\mathcal{B})$	$\log_{10}(A)$ (yr ^{3/2})	β
J1110–5637	PLRN	49.0	$-10.3^{+0.5}_{-0.9}$	$6.5^{+5.7}_{-3.1}$
J1112–6613	PLRN	35.2	$-9.6^{+0.3}_{-0.2}$	$3.5^{+2.8}_{-1.7}$
J1112–6926	WTN	–	–	–
J1114–6100	WTN	–	–	–
J1116–4122	PLRN	4.8	$-13.9^{+3.8}_{-0.8}$	$17.0^{+2.1}_{-5.2}$
J1121–5444	PLRN	111.1	$-9.8^{+0.3}_{-0.3}$	$6.0^{+3.6}_{-2.1}$
J1123–6259	WTN	–	–	–
J1126–6942	WTN	–	–	–
J1133–6250	WTN	–	–	–
J1136+1551	PLRN	6.5	$-10.4^{+0.5}_{-3.9}$	$4.0^{+15.9}_{-2.1}$
J1136–5525	PLRN	174.3	$-10.2^{+0.5}_{-0.6}$	$7.7^{+4.3}_{-2.5}$
J1141–3322	WTN	–	–	–
J1141–6545	PLRN	186.8	$-10.3^{+0.4}_{-0.5}$	$4.7^{+3.2}_{-1.9}$
J1146–6030	WTN	–	–	–
J1157–6224	PLRN	97.5	$-10.1^{+0.2}_{-0.2}$	$3.3^{+1.8}_{-1.4}$
J1202–5820	PLRN	69.2	$-10.3^{+0.4}_{-0.6}$	$5.3^{+4.0}_{-2.0}$
J1210–5559	PLRN	4.5	$-14.7^{+3.2}_{-1.4}$	$13.8^{+6.1}_{-10.4}$
J1224–6407	PLRN	372.6	$-10.7^{+0.2}_{-0.2}$	$5.0^{+1.9}_{-1.5}$
J1231–6303	WTN	–	–	–
J1239–6832	WTN	–	–	–
J1243–6423	PLRN	950.4	$-10.2^{+0.2}_{-0.2}$	$4.5^{+1.0}_{-0.8}$
J1253–5820	PLRN	67.0	$-10.7^{+0.5}_{-0.7}$	$5.6^{+4.5}_{-2.7}$
J1257–1027	WTN	–	–	–
J1259–6741	WTN	–	–	–
J1305–6455	PLRN	197.0	$-9.7^{+0.3}_{-0.6}$	$4.9^{+3.0}_{-1.6}$
J1306–6617	PLRN	7.8	$-11.5^{+1.6}_{-2.6}$	$16.5^{+3.4}_{-12.3}$
J1312–5402	WTN	–	–	–
J1312–5516	WTN	–	–	–
J1319–6056	PLRN	24.8	$-10.3^{+0.4}_{-3.7}$	$3.1^{+15.5}_{-3.4}$
J1320–5359	PLRN	43.1	$-13.8^{+3.1}_{-0.9}$	$19.4^{+0.6}_{-13.4}$
J1326–5859	PLRN	718.2	$-10.1^{+0.3}_{-0.2}$	$5.4^{+1.3}_{-1.0}$
J1326–6408	WTN	–	–	–
J1326–6700	PLRN	107.9	$-9.3^{+0.2}_{-0.2}$	$3.5^{+1.8}_{-1.4}$
J1327–6222	PLRN	946.9	$-9.1^{+0.2}_{-0.2}$	$4.2^{+1.1}_{-1.0}$
J1327–6301	WTN	–	–	–
J1328–4357	PLRN	11.0	$-13.2^{+3.0}_{-0.8}$	$19.9^{+0.0}_{-15.4}$
J1338–6204	WTN	–	–	–
J1350–5115	WTN	–	–	–
J1355–5153	PLRN	4.1	$-13.4^{+2.9}_{-1.0}$	$16.4^{+3.5}_{-11.8}$
J1356–5521	WTN	–	–	–
J1359–6038	PLRN	1556.6	$-10.0^{+0.2}_{-0.1}$	$5.1^{+0.9}_{-0.8}$

Table B1 – *continued*

PSRJ	Model	$\ln(\mathcal{B})$	$\log_{10}(A)$ ($\text{yr}^{3/2}$)	β
J1401–6357	PLRN	693.7	$-9.8^{+0.3}_{-0.3}$	$7.5^{+2.9}_{-2.1}$
J1413–6307	PLRN	143.4	$-9.4^{+0.4}_{-0.3}$	$4.6^{+3.0}_{-2.4}$
J1418–3921	WTN	–	–	–
J1420–5416	WTN	–	–	–
J1424–5822	WTN	–	–	–
J1428–5530	WTN	–	–	–
J1430–6623	PLRN	26.4	$-11.0^{+0.2}_{-0.0}$	$3.2^{+7.2}_{-0.2}$
J1435–5954	WTN	–	–	–
J1452–6036	WTN	–	–	–
J1453–6413	PLRN	156.9	$-10.9^{+0.2}_{-0.2}$	$3.2^{+1.5}_{-1.3}$
J1456–6843	WTN	–	–	–
J1457–5122	WTN	–	–	–
J1507–4352	PLRN	16.2	$-10.3^{+0.4}_{-0.9}$	$3.6^{+5.5}_{-2.5}$
J1507–6640	WTN	–	–	–
J1511–5414	WTN	–	–	–
J1512–5759	PLRN	254.7	$-9.9^{+0.3}_{-0.4}$	$6.8^{+3.9}_{-2.4}$
J1514–4834	WTN	–	–	–
J1522–5829	PLRN	28.9	$-12.3^{+2.1}_{-1.6}$	$11.0^{+9.0}_{-6.3}$
J1527–3931	WTN	–	–	–
J1527–5552	PLRN	11.8	$-10.0^{+0.2}_{-4.1}$	$17.1^{+2.8}_{-15.8}$
J1528–3146*	WTN	–	–	–
J1534–5334	WTN	–	–	–
J1534–5405	PLRN	37.8	$-9.7^{+0.3}_{-0.3}$	$6.1^{+12.2}_{-1.8}$
J1539–5626	PLRN	17.2	$-9.8^{+0.3}_{-0.2}$	$3.1^{+2.7}_{-2.4}$
J1542–5034	PLRN	10.0	$-11.5^{+2.4}_{-0.6}$	$15.3^{+4.6}_{-11.1}$
J1543+0929	WTN	–	–	–
J1544–5308	WTN	–	–	–
J1549–4848	WTN	–	–	–
J1553–5456	WTN	–	–	–
J1555–3134	WTN	–	–	–
J1557–4258	PLRN	10.7	$-12.3^{+1.5}_{-1.2}$	$8.7^{+5.0}_{-5.2}$
J1559–4438	PLRN	5.7	$-10.8^{+0.7}_{-2.7}$	$3.9^{+9.5}_{-0.7}$
J1559–5545	PLRN	221.5	$-8.8^{+0.2}_{-0.2}$	$4.9^{+1.6}_{-1.5}$
J1600–3053*	WTN	–	–	–
J1600–5044	PLRN	270.2	$-10.2^{+0.3}_{-0.4}$	$6.1^{+3.4}_{-2.1}$
J1603–2531	WTN	–	–	–
J1603–2712	WTN	–	–	–
J1603–7202*	WTN	–	–	–
J1604–4909	PLRN	133.1	$-10.3^{+0.3}_{-0.5}$	$5.4^{+2.9}_{-1.4}$
J1605–5257	WTN	–	–	–
J1613–4714	WTN	–	–	–

Table B1 – *continued*

PSRJ	Model	$\ln(\mathcal{B})$	$\log_{10}(A)$ ($\text{yr}^{3/2}$)	β
J1622–4950	PLRN	211.8	$-4.9^{+0.6}_{-0.4}$	$7.3^{+3.4}_{-3.6}$
J1623–0908	WTN	–	–	–
J1623–4256	PLRN	21.2	$-12.6^{+2.3}_{-1.6}$	$19.9^{+0.0}_{-14.2}$
J1626–4537	WTN	–	–	–
J1633–4453	WTN	–	–	–
J1633–5015	WTN	–	–	–
J1639–4604	WTN	–	–	–
J1644–4559	PLRN	2519.7	$-9.9^{+0.2}_{-0.2}$	$6.2^{+1.0}_{-0.9}$
J1646–6831	WTN	–	–	–
J1651–4246	PLRN	125.1	$-12.8^{+2.5}_{-1.2}$	$19.7^{+0.2}_{-12.9}$
J1651–5222	WTN	–	–	–
J1651–5255	PLRN	23.6	$-12.2^{+2.5}_{-1.3}$	$12.6^{+7.3}_{-8.1}$
J1652–2404	WTN	–	–	–
J1700–3312	WTN	–	–	–
J1701–3726	WTN	–	–	–
J1703–1846	WTN	–	–	–
J1703–3241	WTN	–	–	–
J1703–4851	WTN	–	–	–
J1705–1906	PLRN	58.2	$-10.5^{+0.4}_{-0.6}$	$4.8^{+3.9}_{-2.1}$
J1705–3423	PLRN	27.3	$-10.8^{+0.6}_{-3.6}$	$6.2^{+13.7}_{-2.7}$
J1707–4053	WTN	–	–	–
J1708–3426	WTN	–	–	–
J1709–1640	PLRN	48.5	$-9.8^{+0.2}_{-0.4}$	$3.9^{+14.1}_{-1.4}$
J1709–4429	PLRN	504.8	$-9.1^{+0.3}_{-0.4}$	$8.0^{+2.6}_{-1.6}$
J1711–5350	PLRN	8.4	$-12.6^{+2.9}_{-1.0}$	$14.7^{+13.3}_{-11.0}$
J1715–4034	WTN	–	–	–
J1717–3425	PLRN	10.9	$-9.4^{+0.3}_{-2.9}$	$6.2^{+13.7}_{-3.3}$
J1717–4054	PLRN	40.7	$-11.0^{+1.6}_{-2.9}$	$11.4^{+8.6}_{-6.6}$
J1720–1633	WTN	–	–	–
J1720–2933	WTN	–	–	–
J1722–3207	PLRN	6.6	$-13.8^{+3.1}_{-0.8}$	$18.0^{+2.0}_{-13.3}$
J1722–3712	PLRN	372.6	$-9.0^{+0.2}_{-0.2}$	$4.2^{+1.1}_{-0.9}$
J1727–2739	WTN	–	–	–
J1730–2304*	WTN	–	–	–
J1731–4744	PLRN	195.4	$-9.5^{+0.2}_{-0.2}$	$5.0^{+1.5}_{-1.4}$
J1733–2228	WTN	–	–	–
J1736–2457	WTN	–	–	–
J1739–2903	PLRN	19.7	$-13.1^{+2.7}_{-1.1}$	$19.5^{+0.4}_{-14.5}$
J1740–3015	PLRN	128.8	$-8.9^{+0.3}_{-0.2}$	$5.2^{+1.0}_{-1.4}$
J1741–3927	PLRN	159.5	$-9.8^{+0.3}_{-0.3}$	$6.3^{+2.5}_{-1.6}$
J1743–3150	WTN	–	–	–

Table B1 – continued

PSRJ	Model	$\ln(\mathcal{B})$	$\log_{10}(A)$ ($\text{yr}^{3/2}$)	β
J1745–3040	PLRN	68.7	$-14.3^{+3.3}_{-0.7}$	$18.9^{+0.5}_{-5.2}$
J1751–4657	WTN	–	–	–
J1752–2806	PLRN	292.9	$-9.6^{+0.2}_{-0.1}$	$2.9^{+0.8}_{-0.7}$
J1757–2421	WTN	–	–	–
J1759–2205	PLRN	54.9	$-10.1^{+0.3}_{-0.3}$	$4.4^{+2.0}_{-1.6}$
J1759–3107	WTN	–	–	–
J1801–0357	WTN	–	–	–
J1801–2920	WTN	–	–	–
J1803–2137	PLRN	41.3	$-8.6^{+0.5}_{-0.5}$	$17.9^{+2.0}_{-9.8}$
J1805–1504	WTN	–	–	–
J1807–0847	WTN	–	–	–
J1807–2715	PLRN	5.2	$-12.2^{+2.1}_{-1.9}$	$17.0^{+3.0}_{-12.8}$
J1808–0813	WTN	–	–	–
J1809–2109	WTN	–	–	–
J1810–5338	WTN	–	–	–
J1816–2650	WTN	–	–	–
J1818–1422	WTN	–	–	–
J1820–0427	PLRN	99.8	$-10.1^{+0.3}_{-0.5}$	$5.7^{+3.3}_{-2.0}$
J1822–2256	WTN	–	–	–
J1823–0154	WTN	–	–	–
J1823–1115	WTN	–	–	–
J1823–3106	PLRN	33.1	$-10.3^{+0.3}_{-3.5}$	$4.3^{+14.6}_{-4.9}$
J1824–0127	WTN	–	–	–
J1824–1945	PLRN	327.7	$-10.0^{+0.2}_{-0.2}$	$6.1^{+1.2}_{-1.2}$
J1825–0935	PLRN	570.6	$-9.0^{+0.2}_{-0.2}$	$4.9^{+2.1}_{-1.0}$
J1827–0750	PLRN	30.5	$-10.9^{+1.4}_{-1.4}$	$18.8^{+1.1}_{-13.2}$
J1829–1751	PLRN	187.9	$-9.6^{+0.2}_{-0.2}$	$6.0^{+2.6}_{-1.7}$
J1830–1135	WTN	–	–	–
J1832–0827	PLRN	67.8	$-10.4^{+0.6}_{-1.4}$	$6.1^{+7.9}_{-3.0}$
J1833–0338	PLRN	254.7	$-9.6^{+0.2}_{-0.2}$	$5.3^{+1.6}_{-1.1}$
J1833–0827	PLRN	28.4	$-11.9^{+1.8}_{-1.7}$	$15.4^{+4.5}_{-10.5}$
J1834–0426	WTN	–	–	–
J1835–1020	PLRN	84.7	$-8.9^{+0.3}_{-0.1}$	$3.5^{+3.2}_{-1.3}$
J1836–0436	WTN	–	–	–
J1836–1008	PLRN	85.4	$-10.3^{+0.7}_{-0.9}$	$7.8^{+3.5}_{-4.1}$
J1837–0653	WTN	–	–	–
J1840–0809	WTN	–	–	–
J1840–0815	WTN	–	–	–
J1841–0425	WTN	–	–	–
J1841+0912	PLRN	19.3	$-9.8^{+0.4}_{-0.6}$	$4.3^{+4.2}_{-2.5}$
J1842–0359	WTN	–	–	–

Table B1 – continued

PSRJ	Model	$\ln(\mathcal{B})$	$\log_{10}(A)$ ($\text{yr}^{3/2}$)	β
J1843–0000	PLRN	6.3	$-12.7^{+3.0}_{-1.0}$	$19.0^{+0.9}_{-15.2}$
J1844–0433	WTN	–	–	–
J1845–0743	WTN	–	–	–
J1847–0402	PLRN	15.1	$-10.5^{+0.5}_{-4.3}$	$4.3^{+15.6}_{-1.8}$
J1848–0123	PLRN	46.7	$-10.7^{+0.7}_{-3.3}$	$5.7^{+12.0}_{-1.5}$
J1849–0636	PLRN	13.7	$-12.7^{+2.6}_{-1.5}$	$18.2^{+1.7}_{-14.3}$
J1852–0635	WTN	–	–	–
J1852–2610	WTN	–	–	–
J1857+0212	WTN	–	–	–
J1900–2600	WTN	–	–	–
J1901+0331	PLRN	277.3	$-9.5^{+0.2}_{-0.2}$	$4.4^{+1.3}_{-1.3}$
J1901+0716	PLRN	4.1	$-11.4^{+2.3}_{-1.3}$	$17.8^{+2.2}_{-13.9}$
J1901–0906	WTN	–	–	–
J1902+0556	WTN	–	–	–
J1902+0615	WTN	–	–	–
J1903+0135	PLRN	74.4	$-13.4^{+2.5}_{-0.8}$	$20.0^{+0.0}_{-12.4}$
J1903–0632	PLRN	10.2	$-10.1^{+0.3}_{-4.0}$	$2.7^{+16.4}_{-8.1}$
J1905–0056	WTN	–	–	–
J1909+0007	PLRN	64.3	$-10.3^{+0.3}_{-0.5}$	$6.6^{+10.9}_{-1.6}$
J1909+0254	WTN	–	–	–
J1909+1102	PLRN	183.9	$-10.6^{+0.5}_{-0.5}$	$7.9^{+3.5}_{-2.5}$
J1909–3744*†	WTN	–	–	–
J1910–0309	WTN	–	–	–
J1910+0358	WTN	–	–	–
J1913–0440	PLRN	175.6	$-10.9^{+0.6}_{-0.7}$	$7.5^{+5.0}_{-2.4}$
J1913+1400	WTN	–	–	–
J1915+1009	WTN	–	–	–
J1916+0951	PLRN	19.7	$-13.2^{+2.7}_{-1.2}$	$16.5^{+3.5}_{-12.2}$
J1916+1312	PLRN	111.7	$-9.3^{+0.3}_{-0.3}$	$6.0^{+3.3}_{-1.8}$
J1917+1353	PLRN	74.0	$-10.1^{+0.3}_{-0.2}$	$3.7^{+1.9}_{-1.4}$
J1919+0021	WTN	–	–	–
J1926+0431	WTN	–	–	–
J1932+1059	PLRN	206.5	$-10.4^{+0.3}_{-0.2}$	$5.4^{+2.5}_{-1.6}$
J1932–3655	WTN	–	–	–
J1935+1616	PLRN	31.3	$-10.8^{+0.3}_{-2.4}$	$4.5^{+15.5}_{-1.4}$
J1941–2602	WTN	–	–	–
J1943–1237	WTN	–	–	–
J1945–0040	WTN	–	–	–
J1946–2913	WTN	–	–	–
J2006–0807	WTN	–	–	–
J2033+0042	WTN	–	–	–

Table B1 – *continued*

PSRJ	Model	$\ln(\mathcal{B})$	$\log_{10}(A)$ ($\text{yr}^{3/2}$)	β
J2038–3816	WTN	–	–	–
J2046–0421	WTN	–	–	–
J2046+1540	WTN	–	–	–
J2048–1616	WTN	–	–	–
J2051–0827*	WTN	–	–	–
J2053–7200	WTN	–	–	–
J2116+1414	WTN	–	–	–
J2129–5721*	WTN	–	–	–
J2144–3933	WTN	–	–	–
J2145–0750*	PLRN	33.1	$-11.3^{+0.3}_{-0.3}$	$4.8^{+3.3}_{-2.7}$
J2155–3118	WTN	–	–	–
J2222–0137*	WTN	–	–	–
J2241–5236*	PLRN	8.7	$-12.1^{+0.3}_{-0.3}$	$0.4^{+2.0}_{-0.4}$
J2248–0101	WTN	–	–	–
J2324–6054	WTN	–	–	–
J2330–2005	WTN	–	–	–
J2346–0609	PLRN	49.1	$-12.7^{+2.4}_{-1.3}$	$19.1^{+0.9}_{-13.7}$